Thermochimica Acta 726 (2023) 179552

Contents lists available at ScienceDirect

Thermochimica Acta

journal homepage: www.elsevier.com/locate/tca

Review

Thermochemical reduction of iron oxide powders with hydrogen: Review of selected thermal analysis studies

Quentin Fradet *, Michalina Kurnatowska, Uwe Riedel

German Aerospace Center (DLR), Institute of Low-Carbon Industrial Processes, Walther-Pauer-Straße 5, Cottbus 03046, Germany

ARTICLE INFO

Keywords:
Iron oxide
Hydrogen reduction
Thermodynamics
Thermal analysis
Kinetic models

ABSTRACT

The reduction of iron oxide with hydrogen is a much-studied research topic, whose interest is growing even more with the emergence of new applications, for example the hydrogen-based direct reduction or for the production of a carbon-free chemical energy carrier. But the numerous works on this topic reveal the great disparity in the authors' findings, especially regarding the reduction of powders. And while many authors point out this issue, no attempt has been made to converge towards a common understanding of this heterogeneous thermochemical conversion. The endeavor of the present review is to identify the points of consensus, and where discrepancies exist, to explain them. The first part starts with a revision of the latest recommendations on the thermodynamics of iron and its oxides, easing the further comprehension of the reduction process. Then, twelve publications meeting specific criteria on the sample type and reducing agents are systematically confronted. The types of experiments and major experimental conditions have been listed, leading to the identification of typical profiles. Furthermore, chemical pathways are proposed based on these observations and supported by various analytical measurements. Finally, the multiple mathematical approaches to derive kinetic models are compared and discussed. This present review points out the need for appropriate experimental conditions to derive the intrinsic chemistry of the reduction, such as the limitation of water vapor, and also emphasizes the need for more detailed chemical mechanisms.

1. Introduction

The literature devoted to the reduction of iron oxide is abundant. Patisson et al. [1] reported about twenty thousand publications listed by the Web of Science [2] on this topic over the time period 1900–2020. This research has been driven by the economic and academic importance of the field, mostly for its application in the iron and steel industry. The number of publications on the reduction of iron oxide involving exclusively hydrogen amounted 109. This number may seem much smaller than the three thousand papers on the reduction with carbon monoxide, but it conceals the current, rapidly growing interest in hydrogen ironmaking. The same search two years later now gives 168 results. The recent review articles [3–6] on hydrogen-based ironmaking are also evidence of this research direction change.

The primary reason behind this dynamic research activity is the problematic contribution of the steel industry to the anthropogenic greenhouse gas emissions. Mitigation of these emissions is of utmost importance, as the global steel industry accounts for about 9% of the global anthropogenic emissions [7]. More and more research and development programs are dedicated to the transition from the current carbon-based reduction in blast furnaces to the hydrogen-based reduction. While direct reduction using natural gas is seen as a bridging technology, the reduction using green hydrogen has the highest potential, with up to 95% of CO_2 mitigation [8].

The other reason is the emergence of new fields of research involving iron oxide reduction, for example the use of iron as oxygen and/or energy carrier. The ability of iron/iron oxide to be thermochemically reduced and further re-oxidized is at the center of multiple applications [9]. Iron as a solid oxygen carrier represents an attractive option in chemical looping combustion [10–12], where a primary fuel is oxidized with iron oxide to efficiently separate CO_2 from the stream of air. In the steam-iron process [13–16] or in chemical looping hydrogen generation [17–19], iron is oxidized with water steam to generate, store, or purify hydrogen. The ability of iron to generate high-temperature heat through combustion for electricity generation is also being actively investigated [20–22]. According to Bergthorson, iron burns in a heterogeneous combustion mode with air, making it the preferred choice among the metal fuels [23].

* Corresponding author.
E-mail address: quentin.fradet@dlr.de (Q. Fradet).

https://doi.org/10.1016/j.tca.2023.179552
Received 27 March 2023; Received in revised form 8 June 2023; Accepted 9 June 2023
Available online 13 June 2023

The ability of iron to store energy durably, to be easily transported, and to later release this energy, is at the center of the Clean Circles [24] project. The overall process is depicted in Fig. 1. In the storage step, energy is stored via the reduction of iron oxide. This reduction can be electrochemical, or thermochemical with hydrogen produced from renewable electricity. The storage step can be performed in regions with high renewable energy potentials. The energy is now stored in iron, a cheap non-toxic material with a very high volumetric energy density. In the energy release step, iron is oxidized with air, producing heat and giving back iron oxide. The oxidation can be performed in fluidized beds or through dust firing. In this last scenario, coal power plants could be retrofitted to operate with iron powders. Both steps can be repeated and thus constitute a closed carbon-free chemical energy cycle.

The energy storage, i.e. reduction, step of the process is as important as the energy release step. A high process efficiency is required to ensure the viability of the entire process. The reduction in shaft furnaces with iron oxide in the form of pellets is the most mature technology, with a technology readiness level of about 7 [25–27]. However, ongoing research is exploring novel technologies that use iron oxide fines directly, such as entrained-flow or flash reactors [28,29], as well as fluidized-bed reactors [30,31]. The advantages would be, on the one hand, to achieve a higher efficiency of the reduction process and, on the other hand, in the case of iron as an energy carrier, to eliminate the need for pre- and post-treatment of the material [32].

Contrary to laboratory thermal analyses, where well-defined temperature or gas composition can be tested, macro-scale reactors display nonuniform conditions. Thus, the design and operation of these reactors necessitate both a thorough understanding of the reduction process and a robust kinetic model. The literature offers a large number of kinetic models for the reduction of iron oxide with hydrogen [33–44]. This raises the question of which method and model should one follow. A deeper insight into the literature reveals the disagreements in the experimental observations and proposed models. *Discrepancies* [36], *considerable discrepancies* [39], *differing opinions* [35], *results are contradictories* [34]. *Despite extensive research on reduction of iron oxides in literature, there is no consensus on the most accurate reduction kinetics, especially for micron-sized iron oxide powders with high purity* [44].

For these reasons, the present article tackles the comparison and confrontation of studies dealing with the reduction of iron oxide particles with hydrogen. The next section deals with the thermodynamics of iron and iron oxides, as most of the reduction process can be understood through the prism of the stability region. In the following sections, the focus is mostly put on twelve selected papers on the topic of interest. These publications usually follow the same structure. The authors have purchased or prepared an iron oxide sample, generally hematite. A thermal analysis has been performed, usually using thermogravimetric analysis (TGA) or temperature-programmed reduction (TPR), and the results, i.e. the reduction degree over the time or the temperature, are reported. Finally, a kinetic analysis is performed, mostly using an isoconversional method, leading to the determination of an activation energy. Section 3 lists the experiments and the operating conditions of the twelve selected studies [33–44]. The comparison of the curve profiles for various operating conditions has led to a classification of the literature results. Section 4 further analyzes the influence of the sample characteristics, as well as the morphological changes that occur during the reduction process. In the Section 5, chemical pathways are proposed based on these observations and supported by various analytical measurements made by the authors. Finally, Section 6 summarizes the various kinetic results given by the authors and discusses the mathematical methods applied.

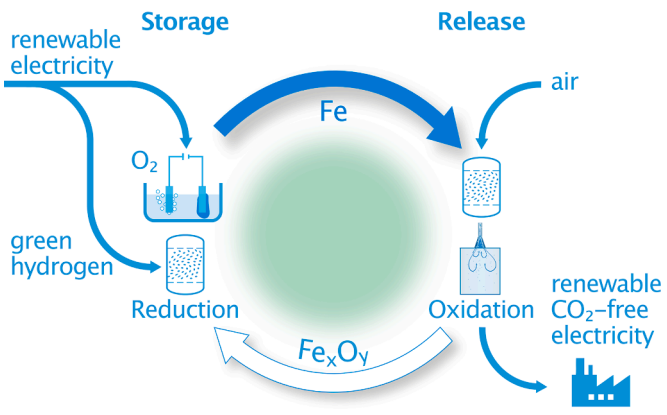

Fig. 1. Renewable electricity is used to reduce iron oxide (storage). At a different place and time, the iron is oxidized again to take out thermal energy for electricity generation (release). Reprinted from Debiagi et al. [20], Copyright 2022, with permission from Elsevier.

2. Thermodynamics of the Fe–O–H system

The study of the thermodynamics of iron and iron oxides enables further comprehension of the reduction process [4,6]. The phase stability diagram of the Fe–O–H is given in Fig. 2. This phase diagram, also called Chaudron diagram or Baur–Glaessner diagram [1], offers an efficient representation of the stability regions of the solid species as a function of the temperature and the hydrogen partial pressure. This amount of hydrogen in the gas is commonly referred to as the gas utilization degree.

Iron has three main oxides, namely hematite Fe_2O_3, magnetite Fe_3O_4, and wüstite $Fe_{1-x}O$. The composition of wüstite is variant and therefore traditionally written as just mentioned. In Fig. 2, its composition was set to $Fe_{.932}O$. This choice will be explained further. The figure clearly shows that the stability region for iron increases continuously with temperature. Iron, wüstite, and magnetite are all stable at a unique condition of temperature and hydrogen partial pressure, identified by the eutectoid point. Below the temperature of the eutectoid, magnetite is the only stable oxide, while above it, wüstite is stable for certain conditions of gas utilization degree. The hematite stability region is not visible in Fig. 2 because this oxide is already unstable at very low hydrogen levels over the temperature range considered here.

A thermochemical software is commonly used to generate the Baur–Glaessner diagram [45,46]. But it can also be generated manually by means of thermochemical equilibrium calculations, which allow to better catch the final representation and any sources of uncertainty.

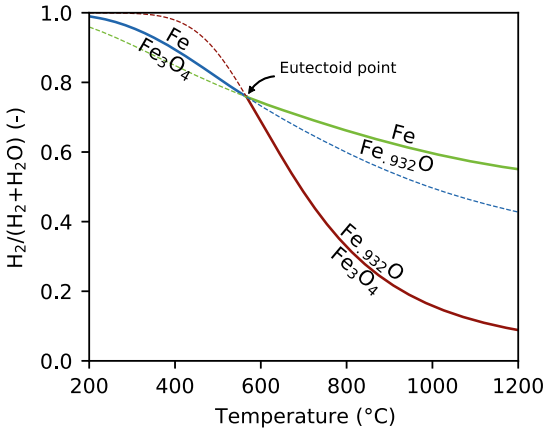

Fig. 2. Phase stability diagram of the Fe–O–H system. The blue, red, and green lines show the partial pressure of hydrogen at the equilibrium as a function of the temperature for the magnetite-iron, magnetite-wüstite, and wüstite-iron reactions, respectively. The solid lines separate the stability region of iron, magnetite, and wüstite. The eutectoid point corresponds to a temperature of 567 °C and a hydrogen partial pressure of 75.8%. (For interpretation of the references to color in this figure legend, the reader is referred to the web version of this article.)

Taking the magnetite/iron system as an example, the reaction linking both species can be written:

$$\frac{1}{4}\,Fe_3O_4 + H_2 \rightleftharpoons \frac{3}{4}\,Fe + H_2O. \quad (1)$$

The former reaction is at chemical equilibrium at a certain temperature T when the Gibbs free energy of reaction is zero, $\Delta_r G(T) = 0$, and the standard Gibbs free energy of reaction follows:

$$\Delta_r G^\circ(T) = -RT\ln K(T), \quad (2)$$

where R is the gas constant and K is the equilibrium constant. The standard free energy of reaction is further related to the standard enthalpy of reaction $\Delta_r H^\circ(T) = \sum_k \nu_k\,\Delta_f H_k^\circ(T)$ and the standard entropy of reaction $\Delta_r S^\circ(T) = \sum_k \nu_k\,\Delta_f S_k^\circ(T)$ by the relation:

$$\Delta_r G^\circ(T) = \Delta_r H^\circ(T) - T\Delta_r S^\circ(T) \quad (3)$$

By expressing the equilibrium constant of Eq. (1) with the partial pressures of hydrogen and water, we get:

$$\frac{P_{H_2O}}{P_{H_2}} = \exp\left(-\frac{\Delta_r H^\circ(T) - T\Delta_r S^\circ(T)}{RT}\right), \quad (4)$$

from which we can deduce the gas utilization degree as a function of temperature:

$$\frac{P_{H_2}}{P_{H_2}+P_{H_2O}} = \frac{1}{1+\exp\left(-\frac{\Delta_r H^\circ(T) - T\Delta_r S^\circ(T)}{RT}\right)} \quad (5)$$

The same expression is obtained with the following three reactions:

$$3\,Fe_2O_3 + H_2 \rightleftharpoons 2\,Fe_3O_4 + H_2O, \quad (6)$$

$$\frac{1-x}{1-4x}\,Fe_3O_4 + H_2 \rightleftharpoons \frac{3}{1-4x}\,Fe_{1-x}O + H_2O, \quad (7)$$

$$Fe_{1-x}O + H_2 \rightleftharpoons (1-x)\,Fe + H_2O, \quad (8)$$

In the end, the profile of the stability regions in Fig. 2 depends only on the choice of the standard enthalpy and entropy of the reactions. But the thermodynamic data of iron and its oxides are difficult to determine accurately, and thus come with a certain uncertainty. The NIST-JANAF thermochemical tables [47,48] are often used, but the thermodynamic properties of the JANAF review for iron and its oxides were last updated in 1978.

The OECD has published a review entitled *Chemical thermodynamics of iron A* [49], which contains recommendations for the choice of the thermodynamic data for iron and its oxide, based on a critical assessment of published information. For iron, the recommendation is to use the values from the review of Desai [50]. For hematite, magnetite and wüstite, the authors conducted their own review of the available data. The recommended data for iron and the oxides were used to produce Fig. 2, while the GRI3.0 data [51] were used for hydrogen and water vapor. For simplicity and consistency with the gaseous species, the recommended thermodynamic data of the OECD were fitted to NASA polynomials [52]. These polynomials take the form:

$$\frac{C_{P,k}^\circ(T)}{R} = a_0 + a_1T + a_2T^2 + a_3T^3 + a_4T^4, \quad (9)$$

$$\frac{\Delta_f H_k^\circ(T)}{RT} = a_0 + \frac{a_1}{2}T + \frac{a_2}{3}T^2 + \frac{a_3}{4}T^3 + \frac{a_4}{5}T^4 + \frac{a_5}{T}, \quad (10)$$

$$\frac{\Delta_f S_k^\circ(T)}{R} = a_0\ln(T) + a_1T + \frac{a_2}{2}T^2 + \frac{a_3}{3}T^3 + \frac{a_4}{4}T^4 + a_6, \quad (11)$$

Table 1
Proposed NASA polynomials to calculate the thermodynamics properties of iron and its oxides .

Species	Temperature range / K	a_0	a_1	a_2	a_3	a_4	a_5	a_6
Fe_2O_3	[298.15, 850]	2.61729398E + 00	4.20598101E − 02	− 2.22685705E − 05	− 3.70207634E − 08	3.83168423E − 11	− 1.01777798E + 05	− 1.56994839E + 01
Fe_2O_3	[850, 955]	1.68251519E + 03	− 9.19768320E + 00	1.85371494E − 02	− 1.62772004E − 05	5.28385649E − 09	− 3.37236385E + 05	− 7.55788361E + 03
Fe_2O_3	[955, 975]	6.92489897E + 05	− 2.14261896E + 03	2.20995541E + 00	− 7.59830854E − 04	0.00000000E + 00	− 1.67962002E + 08	− 3.49260235E + 06
Fe_2O_3	[975, 1100]	2.47252937E + 03	− 6.93190409E + 00	6.52658863E − 03	− 2.04922273E − 06	0.00000000E + 00	− 7.57124284E + 05	− 1.26975884E + 04
Fe_2O_3	[1100, 3000]	1.70916526E + 01	0.00000000E + 00	0.00000000E + 00	0.00000000E + 00	0.00000000E + 00	− 1.04383860E + 05	− 8.76797120E + 01
Fe_3O_4	[298.15, 740]	3.82469045E + 00	5.69085403E − 02	− 2.70781490E − 06	− 1.26634581E − 07	1.19018732E − 10	− 1.37649209E + 05	− 2.02083041E + 01
Fe_3O_4	[740, 847.57]	2.23442015E + 04	− 1.19262966E + 02	2.38712553E − 01	− 2.12166584E − 04	7.06823598E − 08	− 3.47986100E + 06	− 1.01327451E + 05
Fe_3O_4	[847.57, 860]	− 5.30054628E + 01	− 6.71418489E − 02	8.19572230E − 04	− 5.91738213E − 08	− 7.81285922E − 10	− 1.41642421E + 05	2.75351760E + 02
Fe_3O_4	[860, 1040]	3.88765019E + 04	− 1.60652171E + 02	2.48883815E − 01	− 1.71191829E − 04	4.41088229E − 08	− 7.65168930E + 06	− 1.86255226E + 05
Fe_3O_4	[1040, 1870]	2.45369257E + 01	0.00000000E + 00	0.00000000E + 00	0.00000000E + 00	0.00000000E + 00	− 1.40723022E + 05	− 1.22352862E + 02
$Fe_{.932}O$	[298.15, 1000]	4.16156123E + 00	9.86126603E − 03	− 1.77356756E − 05	1.53248312E − 08	− 4.95273744E − 12	− 3.35389654E + 04	− 1.91701052E + 01
$Fe_{.932}O$	[1000, 1652]	6.04388238E + 00	5.62208355E − 04	5.31547086E − 08	0.00000000E + 00	0.00000000E + 00	− 3.38607075E + 04	− 2.78979839E + 01
α − Fe	[298.15, 1000]	5.32161918E + 00	− 2.31955387E − 02	7.69124479E − 05	− 9.73594557E − 08	4.48710837E − 11	− 1.06396887E + 03	− 2.27941375E + 01
α − Fe	[1000, 1043]	− 7.54409933E + 01	8.19911497E − 02	0.00000000E + 00	0.00000000E + 00	0.00000000E + 00	3.73771347E + 04	4.47128379E + 02
α − Fe	[1043, 1060]	1.72886068E + 06	− 4.45486325E + 03	3.34563841E + 00	− 2.24235278E − 04	− 3.95088930E − 07	− 4.81566432E + 08	− 8.98698119E + 06
α − Fe	[1060, 1185]	2.67615995E + 04	− 9.31264019E + 01	1.21576443E − 01	− 7.05543659E − 05	1.53562809E − 08	− 6.15368158E + 06	− 1.32837426E + 05
γ − Fe	[1185, 1667]	3.58685861E + 00	− 6.28121792E − 04	1.18014939E − 06	− 2.62802283E − 10	0.00000000E + 00	− 1.53970727E + 02	− 1.61851091E + 01

where $a_0, \ldots, a_6$ are the fitted numerical coefficients. Several sets of coefficients are needed for each solid species to accurately retrieve the tabulated values for the temperature range of interest. The fitted values are given in Table 1 and the heat capacity is plotted versus temperature in Fig. 3. The heat capacity of iron, magnetite, and iron has a peak corresponding to a λ-transition.

Wüstite is the oxide, whose thermodynamic data are the most difficult to define. Wüstite is an iron-deficient Fe^{II}, thus generally written $Fe_{1-x}O$, and is also metastable below a certain eutectoid temperature, T_C, which means that a choice has to be made regarding the composition of wüstite and extrapolation is needed to determine its properties below T_C. Many studies have been devoted to defining detailed compositions and thermodynamic properties for wüstite [53–55]. Here, the OECD recommendations were followed with the unique composition for wüstite, $Fe_{.932}O$ and $T_C = 567$ °C. Three methods have been proposed for calculating the standard enthalpy of formation of wüstite at the standard temperature. The first method uses the fact that at the eutectoid point, the free Gibbs energy of the following reaction:

$$Fe_3O_4 + (1-4x)\ Fe \rightleftharpoons 4\ Fe_{1-x}O, \tag{12}$$

is zero, which results in:

$$\Delta_r H^\circ(T^\circ) = \int_{T^\circ}^{T_C} \Delta_r C_P^\circ\ dT + T_C \Delta_r S^\circ(T^\circ) + T_C \int_{T^\circ}^{T_C} \frac{\Delta_r C_P^\circ}{T}. \tag{13}$$

Knowing the heat capacity of wüstite from T° to T_C and the standard entropy of wüstite at T° allows the evaluation of Eq. (13), and thus of the standard enthalpy of formation of wüstite at the standard temperature:

$$\Delta_f H^\circ_{Fe_{1-x}O} = \frac{1}{4}\left[\Delta_r H^\circ(T^\circ) + \Delta_f H^\circ_{Fe_3O_4} + (1-4x)\Delta_f H^\circ_{Fe}\right]. \tag{14}$$

The derivation of this property permits the plotting of the phase diagram in Fig. 2. Therefore, one should not misinterpret and conclude that the eutectoid temperature can be deduced by reading the diagram from a priori independent thermodynamic properties. The prior assumption of the eutectoid temperature led to the determination of the thermodynamic data and thus to the generation of the phase diagram. Therefore, although this phase diagram is useful for interpreting the reduction process, it is associated with certain uncertainties, especially because of the complexity of wüstite.

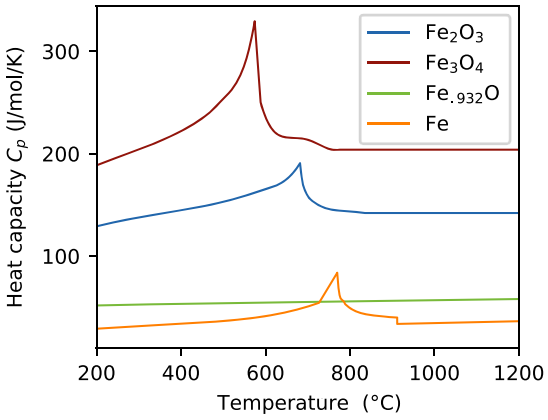

Fig. 3. Heat capacities of iron and its oxides versus the temperature. Their values have been calculated with the NASA coefficients given in Table 1, which are themselves based on an all-encompassing review [49].

3. Experiments

The intent of this section is to provide an overview of the most relevant thermal analysis experiments that have been conducted on the reduction of iron oxide powders with hydrogen. This is achieved by listing the relevant publications and specifying the type and number of experiments, as well as the main experimental conditions. Later in this

Table 2
Thermochemical analysis studies on the reduction of iron oxide powders with hydrogen.

Publication	Number and type of experiments	Temperature C or Heating rate C/min	Gas composition [%]	Flow rate [cm^3/min]	Sample mass [mg]	Sample
Pineau et al. [33]	15 isothermal TGA	218–515	100 H_2	1667	100	A
2006	6 isothermal TGA	341–586	10/90 H_2/N_2	1667	100	A
Pineau et al. [34]	13 isothermal TGA	227–426	100 H_2	1667	100	A
2007	19 isothermal TGA	218–952	100 H_2	1667	100	B
Jozwiak et al. [35]	10 TPR	0.58–10.7	5/95 H_2/Ar	50	15 ; 50	A
2007	10 TPR	0.58–10.7	5/95 H_2/Ar	50	15?	B ; C
	3 linear DTGA	5	100 H_2	50?	10	A - C
	2 phase compositions	1	5/95 H_2/Ar	50?	200	A ; C
Tiernan et al. [36]	2 TPR	10	5/95 H_2/He	52	2	A ; B
2001	2 CRTPR	− 10 − 5	5/95 H_2/He	52	2	A ; B
Shimokawabe et al. [37]	12 linear TGA	4.5	0.2 bar 33/67 H_2/N_2	?	30	A - L
1979	10 isothermal TGA	275–450	0.2 bar 33/67 H_2/N_2	?	30	A ; D
Peña et al. [38]	1 TPR	5	5/95 H_2/N_2	100	200	A
2006	1 linear TGA	5	5/95 H_2/N_2	750	20	A
	9 isothermal TGA	360–440	10–90/90–10 H_2/N_2	750	20	A
Lorente et al. [39]	12 isothermal TGA	400	50/0–5/45–50 $H_2/H_2O/N_2$	750	20	A ; B
2011	4 redox cycles	400	50/0–5/45–50 $H_2/H_2O/N_2$	750	20	A
Wimmers et al. [40]	3 TPR	0.2	67/33 H_2/Ar	16	3.6 ; 8.2 ; 15.9	A
1986	5 TPR	0.2–10	67/33 H_2/Ar	16	0.08–3.6	A
	5 TPR	0.2–10	67/33 H_2/Ar + 3 H_2O	16	0.17–7.0	A
Piotrowski et al. [41]	1 isothermal TGA	700	100 H_2	30	13	A
2005	4 isothermal TGA	700–910	10/90 H_2/N_2	30	13	A
Viswanath et al. [42]	2 isothermal TGA	255	100 H_2 Ø Nitrogen trap	?	200	A
1975	1 isothermal TGA	395	100 H_2+H_2O	?	200	A
Zieliński et al. [43]	4 TPR	5	0;0.6;1.2/5.8;83.6 H_2O/H_2+Ar	30	5	A
2010	4 TPR	5	0;0.6;1.2/5.8;83.6 H_2O/H_2+Ar	30	25	A
	2 TPR	10	0;2.5/83.6 H_2O/H_2+Ar	30	50	A
Hessels et al. [44] 2022	14 isothermal TGA	400–900	25–100/75–100 H_2/N_2	150–480	150	A

section, the results of these experiments are concisely summarized by means of characteristic curves. When a figure from the literature is mentioned, the word *Figure* is written in italic to distinguish it from the figures of this paper.

The selected thermal analysis studies are listed in Table 2. This section and those that follow will focus primarily on these studies, although further sources will be considered where appropriate. Publications have been included in the table only if they contain experiments that meet the following criteria:

- the initial sample is an iron oxide of high purity,
- the size of the particles is in the micrometer range,
- the sole reducing agent of the injected gas is hydrogen.

This excludes a major part of the literature as iron ore [56–58] or doped oxides [59–61], are typically used, in the form of pellets [62–65], and in the presence of carbon monoxide [66,67]. The idea is to restrict the focus to the experiments that can capture the intrinsic chemistry of the iron oxide reduction with hydrogen, without being hindered by transport considerations [68] or further chemical pathways [69]. It is uncertain whether the study of Vidwanath et al. [42] listed in Table 1 was performed using pellets or not. In another study [70] published two years later, the research group specified "cylindrical pellets of the oxide [...] prepared by compression". Despite the doubt, this publication was included in the table because many of the selected works [33,36,39,40] referred to its conclusions applied to the case of iron oxide powders.

For the sake of simplicity, the terms *isothermal TGA* and *linear TGA* are employed in Table 1 and across this paper to designate thermogravimetric analysis performed under isothermal conditions or with linear heating rates. The acronym DTGA is used when differential values of the mass evolution were given by the authors. The term *temperature-programmed reduction* is somewhat misleading, because it could as well be applied to TGA experiments under temperature-programmed mode. Authors employed this term to refer to experiments in which gas consumption or production is measured rather than the mass evolution. The term *evolved gas analysis* could be more explicit. However, *temperature-programmed reduction* or *TPR* is used throughout this review for the sake of consistency with the terminology of the literature. The table illustrates the high number of experimental tests already performed. Most authors relied on isothermal TGA, linear TGA or TPR. Atypical experiments include the constant rate TPR or *rate-jump* experiments from Tiernan et al. [36], redox cycles from Lorente et al. [39], and X-Ray phase compositions obtained over the course of reduction experiments under a linear heating rate from Jozwiak et al. [35].

TPR, linear and isothermal TGA are present in 5, 3 and 9 publications, respectively, thus providing a better point of comparison than the other experiments. Experimental results from different groups, or even within the same group, can show very distinct profiles, due to the variety of factors influencing the reduction. Some are hardly quantifiable, for example the choice of the crucible shape, the crucible material, or the flow structure within the measurement furnace. But there are fundamental experimental parameters, which are quantitative and comparable between experiments. These parameters are given in Table 2 and are the temperature or heating rate (HR), the gas composition (pure or diluted hydrogen, with or without added steam), the gas flow rate (FR), and the mass of the sample (m_s). The linear gas velocity inside the furnace may be a better indicator than the volumetric gas flow rate. The rate at which reactants are brought to the sample surface or products are driven away is conditioned by the flow velocity. However, most studies omit the furnace cross sectional area, which prevents access to the information on the velocity. The sample characteristics also play a crucial role, but are more difficult to compare or interpret. Section 4 will be dedicated to reviewing the current knowledge of the sample characteristics on the reduction process.

In terms of results given by the authors, it differs between TPR and TGA. The TPR results are usually given on an axis with an arbitrary unit. Only Zieliński et al. [43] managed to relate their measurements to the percentage of hydrogen or water in the furnace, providing additional information. On the other hand, the raw data of the thermogravimetric studies are usually not reported. Instead of the sample mass over time or temperature, the authors give the degree of conversion α, which takes into account the initial and final mass of the sample, $m_{s,0}$ and $m_{s,\infty}$, and goes from 0 to 1:

$$\alpha(t) = \frac{m_{s,0} - m_s(t)}{m_{s,0} - m_{s,\infty}}. \tag{15}$$

With the definition from above, if a pure hematite sample were hypothetically completely reduced to magnetite and no further, α would be equal to 11.1%. The extent of reduction up to wüstite $Fe_{.932}O$ would amount 28.5% and obviously 100% for a complete reduction to iron. The other way around, the maximum mass loss of the reduction is 30.1% of the initial sample mass.

3.1. Experiments with a linear heating rate

Let us first distinguish the TPR and linear TGA experiments from the isothermal TGA. Both TPR and linear TGA are performed under a linear heating rate, only the measurement differs. In TPR, the water production or the hydrogen consumption is measured, while in linear TGA, the sample mass evolution is recorded. But both measurements are obviously linked and taking the derivative of the TGA results gives a curve typical of a TPR experiment, as shown in Jozwiak et al. [35] and in Tiernan et al. [36].

The comparison of the experiments under linear heating rate conditions led to the identification of 6 typical profiles according to the main experimental parameters. The categories and the associated curves can be seen in Fig. 4; the linear TGA curves in red were obtained by integration of the TPR curves. These typical profiles are not meant to represent specific experimental data, the temperatures given at a certain extent of reaction are only indicative and can vary greatly. This classification comes with inherent flaws, as it cannot convey the complexity of the individual experiments, but it helps to narrow the focus from hundreds of experiments to a few, and also serves to identify the effect of fundamental parameters. The characteristics of the curves in Fig. 4 (number of peaks, narrow or spread out on the temperature axis) can be quickly related to different experimental conditions, allowing a comprehensive review of the experiments conducted in the literature. The classification process revealed that the most decisive parameters were the concentration of hydrogen (highly diluted in inert gas up to pure hydrogen), the furnace heating rate, the initial mass of iron oxide, the gas flow rate, and the optional addition of water in the feed. In order to limit the number of categories, the aforementioned conditions that appeared to have a similar effect on the course of reduction have been grouped together. The sign & in the boxes in Fig. 4 means that both conditions shift the experiments toward the same typical profile. For example, both increasing the mass of the sample and decreasing the flow rate cause the reduction to spread to high temperatures. Regarding the choice of colors in the boxes, green means that the conditions increase the reduction rate, and red means that they decrease it. At this stage, only a classification based on experimental observations is made, a more detailed explanation will be given in Section 5.

3.1.1. Influence of the hydrogen concentration and the heating rate

To catch the influence of these two parameters, we focus on the Fig. 4 (a) and (b), i.e., at low sample mass and high flow rates in the absence of water in the gas feed.

- Curve 1 in *Figure* 2 of Zieliński et al. [43] illustrates the scenario in Fig. 4(a) A single peak is observed and the reduction is achieved at low temperatures, at about 400 °C. *Figure* 1 curve a of Wimmers et al. [40] constitutes another example of TPR reduction in this category,

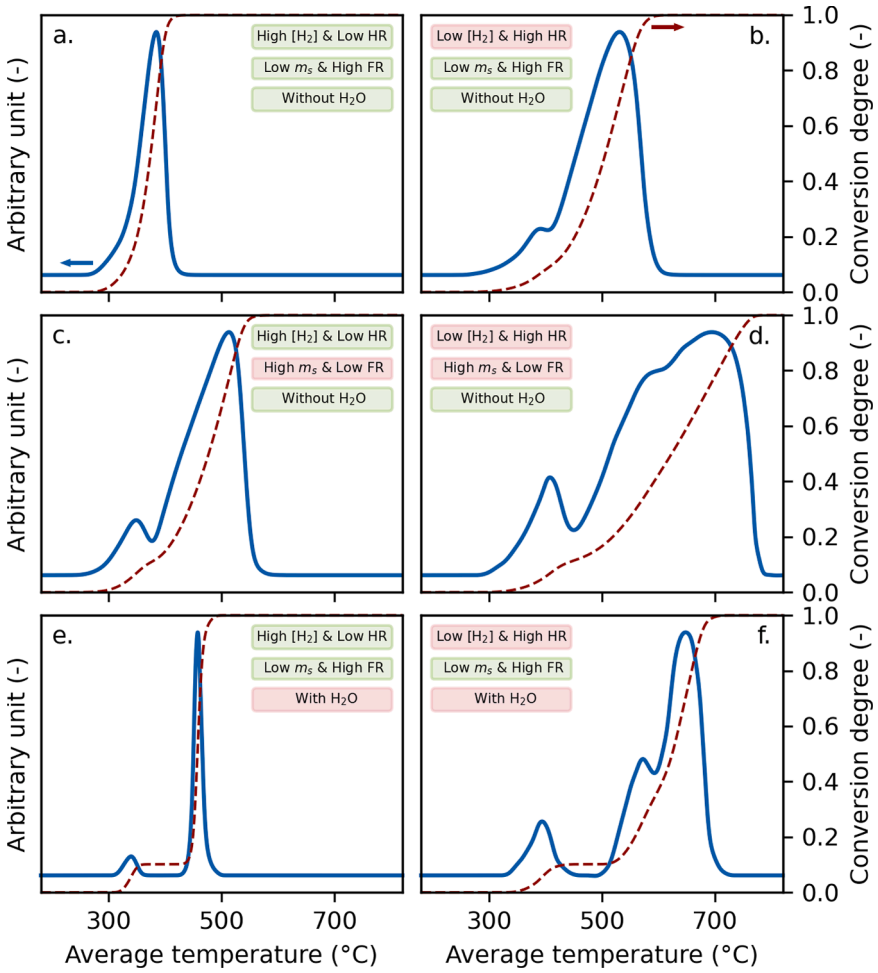

Fig. 4. Typical profiles of TPR (blue lines) and linear TGA (red dashed lines) of hematite reduction following various experimental conditions. These profiles are not real experimental results, rather were drawn from one or more experiments under the conditions indicated in the boxes. (For interpretation of the references to color in this figure legend, the reader is referred to the web version of this article.)

again with a terminal reduction temperature of 400 °C. It should be noted that Jozwiak et al. [35] performed a DTGA experiment under very similar conditions (Zieliński: 5 mg of Fe_2O_3 under a heating rate of 5 °C/min and a gas flow rate of 30 cm^3/min with 83.6% H_2, Jozwiak: 10 mg of Fe_2O_3 under a heating rate of 5 °C/min with 100% H_2), but whose profile is very different and resembles Fig. 4(c). Reasons for this difference could be the value of the flow rate, which is not explicitly given, or be related to the sample or flow configuration.

- Decreasing the hydrogen concentration or increasing the heating rates has a similar effect of spreading the reduction over a larger temperature range. TPR experiments corresponding to Fig. 4(b) are Zieliński et al. [43] *Figure* 2 curve 3, Jozwiak et al. [35] *Figure* 1. B. curves 1–5, and Tiernan et al. [36] *Figure* 3. An example of linear TGA experiment can be seen in Peña et al. [38] *Figure* 4. Under these conditions, two reduction steps can be distinguished, but with significant overlap, and the reduction is achieved at about 500 to 600 °C. The TGA curve shows an inflection point at around 11%, corresponding to the reduction of hematite to magnetite.

3.1.2. *Influence of the sample mass and the flow rate*

Influence of these parameters can be observed by comparing Fig. 4 (a) and (b), with Fig. 4(c) and (d).

- Experiments similar to Fig. 4(c), i.e. with an important sample mass and a low gas flow rate but high hydrogen contents and low heating rates, are Zieliński et al. [43] *Figure* 2 curve 2 and 5 curve 11, Wimmers et al. [40] *Figure* 1 curves b-c, and Jozwiak et al. [35] *Figure* 1. A. curves 1-2. The profiles of the aforementioned experiments could be mistaken with the curves of Fig. 4(b) despite very different experimental conditions.
- When the hydrogen concentration is decreased or the heating rate is increased, the curves are spread to very high temperatures, as shown in Fig. 4(d). In this category, we can mention Zieliński et al. [43] *Figure* 2 curve 4, Jozwiak et al. [35] *Figure* 1. A. curves 3–5, or Peña et al. [38] *Figure* 3(a). The linear TGA data of Shimokawabe et al. [37] shown in *Figure* 1 curves a-b and *Figure* 2 curves a–d are difficult to categorize between Fig. 4(c) and (d). The hydrogen concentration is relatively high, but the operating pressure is only at 0.2 bar. The flow rate was also not specified.

3.1.3. *Influence of the addition of water in the inlet flow*

Some authors tested the addition of water directly in the inlet feed, which led to profiles similar to Fig. 4(e) and (f). Only cases with low mass to flow rate ratios were considered. Zieliński et al. [43] also performed two experiments at high mass to flow ratios with water addition. They were not considered here, as a combination of Fig. 4(d) and (f).

- Wimmers et al. [40] were among the first to study the effect of water on the thermochemical reduction of iron oxides. The curves a-f in their *Figure 2* correspond to the case shown in Fig. 4(e). In all of their experiments, two well-separated peaks are obtained. The reduction

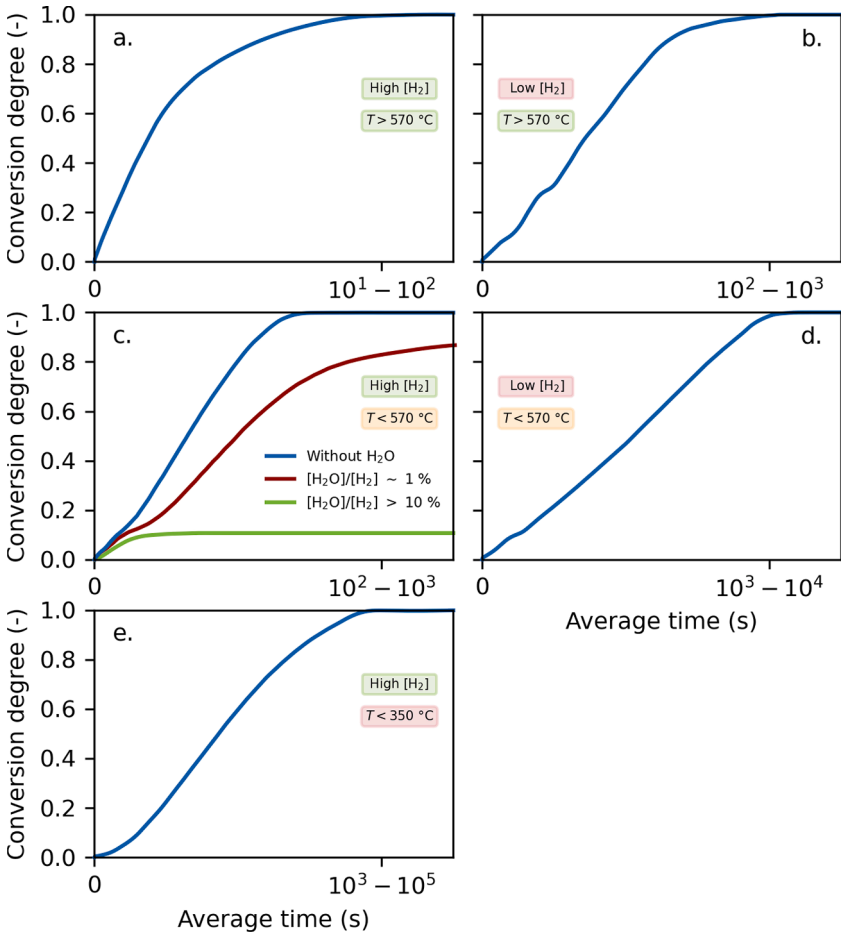

Fig. 5. Typical profiles of TG analyses under isothermal conditions of hematite reduction according to various experimental conditions. These profiles are not real experimental results, rather were drawn from one or more experiments under the conditions indicated in the boxes.

of magnetite to iron begins after the complete reduction of hematite to magnetite. Zieliński et al. [43] found a very similar profile, shown in *Figure* 5 curve 12.

- Zieliński et al. [43] further studied the influence of water at low hydrogen concentrations, as depicted in Fig. 4(f). Their corresponding experimental data can be seen in their *Figure* 3 curves 6 and 7. Under these conditions, 3 peaks can be observed. The second and third peaks may overlap or be separated, depending on the amount of water in the gas stream, and the terminal temperature ranges from 700 to 800 °C.

3.2. *Experiments under isothermal conditions*

A similar review can be performed for the isothermal cases. Typical profiles are shown in Fig. 5. In comparison, the influence of some operating parameters has been less studied. The major operating parameters that have been varied are the temperature and the dilution of the reducing agent. Thus, the retained classification is different temperature ranges and hydrogen concentrations.

The most abundant data sources for linear TGA are from namely Pineau et al. [33] and Pineau et al. [34], with 21 and 32 experiments in their first and second publications, respectively. They actually performed many more tests, with variations in sample weight or the gas flow rate, but only the ones explicitly presented in their papers are considered in Table 2. In their paper with hematite as iron oxide, the experiments cover a temperature range of 218 to 586 °C, 15 with pure hydrogen and 6 with a tenfold nitrogen dilution. In many of the experiments, an inflection point is visible around 11% conversion degree, as in Fig. 5(c) and (d), while their unique experiment above the eutectoid temperature shows 2 inflection points, as in Fig. 5(b). At comparable temperatures, the dilution of hydrogen by a factor of ten increases the reduction time by about 5. At very low temperatures, an inflection point is barely visible and resembles Fig. 5(e), for example their experiments at 233, 237, 258, and 308 °C. However, the test at 218 °C clearly shows two steps.

Piotrowski et al. [41] also tested hematite reduction above 570 °C with pure hydrogen and with a tenfold dilution by nitrogen. Their test with pure hydrogen corresponds to Fig. 5(a), with no inflection point. Their tests with diluted hydrogen are difficult to characterize, because only the initial reduction portion is given. Their conversion degree was calculated on the basis of the reduction of hematite to wüstite only. However, no clear inflection point is visible in this initial reduction range. This could be attributed to the higher mass to flow rate ratio than in Pineau et al. [33], which shifts the reduction towards a diffusion limited process.

Peña et al. [38] performed isothermal experiments at temperatures between 360 to 440 °C and gas compositions from 10/90 to 90/10% H_2/N_2, and whose profiles correspond well with Fig. 5(c) and (d).

The isothermal experimental results of Viswanath et al. [42] should be taken with more caution, because as mentioned earlier, they may have used pellets [70] rather than powders. This is also not specified in another regularly cited article [60] with doping agents. Many data were not given in full, rather derived results were presented, such as the reduction rate, without specifying whether this was the initial or maximum rate. They came to the conclusion that the reduction rate increases between 2 and 7.5% of water vapor in the inlet feed for tests

between 465 and 505 °C. Even more, they came to the conclusion from experiments at 255 °C that the reduction does not proceed beyond the stage of Fe_3O_4 when all the water vapor is removed.

This is in obvious contradiction with the linear tests mentioned previously, which showed the adverse influence of water addition, but also with the isothermal runs of Lorente et al. [39] In their study, isothermal TGA tests at 400 °C were performed with varying amounts of water vapor in the feed. Their results show that increasing the water content drastically slows down the reduction, and especially the second step from magnetite to iron, as depicted in Fig. 5(c). Above a certain amount of water (in their test 5/50/45% $H_2O/H_2/N_2$), the reduction does not proceed any further, which can be easily understood from the thermodynamic phase diagram, Fig. 2.

Hessel et al. [44] recently performed isothermal reduction experiments on combusted iron particles. All of their curves, even at temperatures below 570 °C, look similar to Fig. 5. To what extent the material tested differs from the regular samples used in the literature is uncertain. The absence of an inflection point from hematite to magnetite could be attributed to the fact that the sample initially contains a large amount of magnetite (58%).

Finally, Shimokawabe et al. [37] carried isothermal TGA in the temperature range of 275–450 °C with two different samples. It was shown that depending on the sample characteristics, the curve profiles can vary greatly. This is further detailed in the next section.

4. Sample characteristics

Information relevant to the sample characteristics of the reviewed publications is listed in Table 3. Many authors used a single hematite sample, but magnetite samples were also considered and even one wüstite sample [35]. About half of the samples were obtained from commercial suppliers, the other half were prepared from salts. The sample from Hessels et al. [44] has the peculiarity of originating from the combustion of iron particles.

The characterization of the samples is more or less detailed. The average diameter or the diameter range is usually given and the surface areas are derived from the BET method. The samples may or may not be porous. Only two groups of authors [36,40] reported values for the average porosity.

Trying to characterize the influence of the sample characteristics on the reduction is difficult because of differences in the other experimental conditions among multiple authors. Even concerning the particle size diameter, Zieliński et al. [43] used a sub-micron powder and their reduction profiles, are at first sight, very close to the TPR results of Peña et al. [38], who used a sample with particle diameters above 100 µm.

Two research groups studied the influence of sample characteristics, or sample preparation, on the reduction behavior, while keeping the same experimental setup. Shimokawabe et al. [37] conducted the most exhaustive study on this aspect. They prepared hematite powders by calcination of seven iron salts in a stream of oxygen, air or nitrogen, in the temperature range of 500–1200 °C. They also studied the effect of doping elements, but this is beyond the scope of the present review.

They were able to show that the reactivity of Fe_2O_3 is strongly influenced by the sample characteristics, whereas the reactivity of the Fe_3O_4 formed is almost independent. They used the initial reduction temperature as an indicator of reactivity in the case of linear TGA. This initial temperature increases, and thus the reactivity decreases, with the sample preparation temperature, with the exception of a slight decrease around 700 °C. They could further relate this indicator to the particle characteristics. According to Shimokawabe et al. [37], the initial reduction temperature increases almost linearly with an increase in the crystallite size, and seems inversely proportional to an increase in the specific surface area. Their isothermal experiments confirmed the previous results. Tests with hematite prepared at low temperatures showed a neat inflection point because of a high hematite reactivity. On the contrary, the sample prepared at high temperatures has a much lower initial reactivity. However, after this inflection point, the reactivity of both samples is similar.

Pineau et al. [34] performed similar tests by using two samples with distinct preparation temperatures, but with magnetite. Their sample prepared at 1200 °C has a diameter about ten times larger than the one prepared at 600 °C, while the surface area is about 7 times smaller. The magnetite characteristics seem to play a limited role, as at temperatures lower than 400 °C, the reaction rates of the two solids are almost identical. They noted, however, that at temperatures higher than 600 °C, the behavior of the two solids is different.

In general, it appears that samples prepared at lower temperatures favor the reduction by featuring a higher contact surface with the gas

Table 3
Samples used in the thermochemical analyses listed in Table 2.

Publication	Sample	Solid composition	Origin	Diameter [µm]	Surface area [m^2/g]	Porosity [cm^3/g]
Pineau et al. [33] 2006	A	99.8% Fe_2O_3	Commercial (Merck)	1–2	0.51	3.3
Pineau et al. [34]	A	Fe_3O_4	Fe_2O_3 600 °C in H_2/H_2O	1–2	0.7	
2007	B	Fe_3O_4	Fe_2O_3 1200 °C in H_2/H_2O	10–20	0.1	
Jozwiak et al. [35]	A	Fe_2O_3	$Fe(NO_3)_3{\cdot}9H_2O$ 600 °C in air		23.5	
2007	B	Fe_3O_4	Commercial (Aldrich)		5.6	
	C	FeO	Commercial (Aldrich)		1	
Tiernan et al. [36]	A	99.98% Fe_2O_3	Commercial (Aldrich)	< 250	160	0.185
2001	B	99.997% Fe_3O_4	Commercial (Alfa Chemicals)	2	2	0.005
Shimokawabe et al. [37]	A–D	Fe_2O_3	$Fe(OH)(CH_3COO)_2$ 500–1200 °C in air		2.0–13.5	
1979	E–I	Fe_2O_3	$FeSO_2{\cdot}7H_2O$ 700–1200 °C in air		1–13	
	J–L	Fe_2O_3	$Fe(OH)(CH_3COO)_2$ 500–1200 °C in O_2		0.6–15.8	
Peña et al. [38] 2006	A	Fe_2O_3	$Fe(NO_3)_3{\cdot}9H_2O$ 800 °C in air	100–160	2.3	
Lorente et al. [39]	A	Fe_2O_3	$Fe(NO_3)_3{\cdot}9H_2O$ 800 °C in air	100–160	2.3	
2011	B	Fe_3O_4	A in H_2/H_2O			
Wimmers et al. [40] 1986	A	Fe_2O_3	Commercial (Merck)	0.3	2.6	
Piotrowski et al. [41] 2005	A	Fe_2O_3	Commercial (PEA Ridge Iron Ore Co.)	91		
Viswanath et al. [42] 1975	A	Fe_2O_3	$Fe(NO_3)_3{\cdot}9H_2O$ 475 °C			
Zieliński et al. [43] 2010	A	Fe_2O_3	Commercial (Merck no. 4625270)	0.4–0.5	2.2	
Hessels et al. [44] 2022	A	40/58 Fe_2O_3/Fe_3O_4	Fe combusted	5–100	0.330	

phase. However, this effect is difficult to characterize. On top of this, the sample properties evolve during the reduction. There is, of course, the evolution of the solid species, from the oxides to iron. But it is accompanied by morphological changes, which may be beneficial or not. Shimokawabe et al. [37] took SEM images before, during, and after the reduction of one reactive sample, prepared at 500 °C, and one less reactive sample, prepared at 1200 °C. They suggested that their sample prepared at low temperature, featuring small particles, was reduced while keeping its particle shape unchanged. While their SEM images of the sample prepared at high temperature initially showed a large particle with a flat surface, suggesting melting of the oxide, which later took over the reduction a similar shape to the former sample, but with larger particles, explaining the similar rate of reduction in the second step. On the contrary, Pineau et al. noted that sintering occurs over the course of reduction, leading to a decrease in reactivity. In both of their studies [33,34], they stated that the solid starts to sinter above ~390–420 °C and this sintering increases with temperature. They noted even severe sintering above 700 °C. Their TGA results show that even though the initial rate of reduction increases with the temperature, the sintering later hinders the process and a strong decrease in the reduction rate can be observed. In addition, the reduction does not seem to proceed to completion. Similar agglomeration of the powder was reported by Hessel et al. [44] at temperatures above 500 °C.

The matter of the initial porosity of the samples but also of the pores forming during the process has been overall neglected in the selected studies. It is well known that the iron forming from the gaseous reduction of iron ore pellets is highly porous, with hole marks, hence the name sponge iron. Towhidi et al. [71] determined a porosity of about 61% after reduction of a pellet with an initial porosity of 16%. The porous structure of the forming iron was also reported during the reduction of dense wüstite strips. According to Turkdogan et al. [72], lower reduction temperatures favor small but numerous pores and the pore surface area decreases markedly with increasing temperatures. Interestingly, Hessel et al. [44] came to the same conclusion in the case of powders by comparing SEM images before and after the reduction: *it can be observed that the powder becomes porous in all reduction experiments. As the reduction temperature increases, the number of pores decreases, but the pore size increases.*

A better characterization of the role of the solid structure in the reduction is an interesting direction for future research. Highly porous materials could be controlled by pore diffusion as proposed by Kuila et al. On the contrary, solid-state diffusion is particularly important for dense materials. According to Edström et al. [73], hematite reduces faster than magnetite because it gives products that are more porous. Bai et al. [74] studied the influence of pore connectivity and showed that isolated pores in the microstructure are filled with water vapor. They also investigated the mechanical stresses building up, elastic and elasto-plastic deformations, and their effects on the reaction kinetics. Shrinking and swelling also occur during the reduction process. This was investigated by El-Geassy et al. [75] and Yi et al. [76] for compacts and pellets, respectively. Both showed that the reduction with hydrogen involves an initial and moderate step of swelling and a terminal contraction of the iron phase. Ma et al. [77] further showed the strong heterogeneity in a partially reduced hematite pellet by means of synchrotron high-energy X-ray diffraction and electron microscopy. They were able to quantitatively investigate how much spatial gradients, morphology, and internal microstructures impacts the reduction efficiency and metallization.

5. Chemical pathways

It is clear that different conclusions can be drawn depending on the practical conditions of thermal analysis. For instance, since many reduction experiments are completed or near completion at 567 °C, the formation of wüstite is often neglected. Among the 12 papers considered, wüstite is not mentioned a single time in 4 of them. Thus, the generally admitted mechanism is that hematite is reduced stepwise to magnetite and iron. For some authors, both steps are separate, while for others they overlap. For Tiernan et al. [36], *The prereduction step to* Fe_3O_4 *is complete prior to the onset of the main reduction step to metallic iron*. For Peña et al. [38] *The typical shape of the curves, with a shoulder at a degree of reduction of about 10–12%, points to a stepwise reaction via* Fe_3O_4*, with overlapping of two reduction processes*.

To further apprehend the chemical pathways, many authors have performed analytical measurements to supplement the reduction experiments, for example X-ray diffraction (XRD). We can distinguish between ex situ XRD, where the measurement is performed on the raw material, on the product, or on a partially reduced sample that has been quenched, and in situ XRD.

Shimokawabe et al. [37] performed XRD analysis on two samples reduced to 11%. The first sample, with a higher hematite reactivity, consisted entirely of magnetite. The second sample contained hematite, magnetite, and iron. It was therefore demonstrated that both steps, from hematite to magnetite and from magnetite to iron, can either be completely separated or overlap, depending on the reactivity of the individual steps. The simultaneous presence of the three species at 11% of reduction could be found by another group [38]. Under certain circumstances, the overlap can even lead to a single apparent step, from hematite to iron. Zieliński et al. [43] recorded in situ XRD spectra during the reduction of hematite under the conditions in Fig. 4(a), that is conditions that favor very low-temperature reduction. Their measurements suggested the presence of hematite and iron exclusively.

The isothermal runs of hematite reduction at very low temperatures by Pineau et al. [33] might lead to a similar conclusion. The curves below 330 °C, except for the one at 218 °C, do not show a clear plateau around 11%, but rather a single sigmoid. This does not necessarily mean that Fe_3O_4 does not form, but suggests that the rate of reduction of both steps is similar. The authors performed in situ XRD, but did not detail their results for this temperature range, rather for higher temperatures, where they detected wüstite.

Their X-ray diffraction results in the temperature range of 450–570 °C revealed the presence of wüstite, with crystal parameters corresponding to almost stoichiometric FeO. In their second publication [34], stoichiometric wüstite was found during the reduction of magnetite samples at temperatures as low as 390 °C. This seems to contradict thermodynamic considerations, as shown in Fig. 2. But the authors noted that this is possible *under irreversible thermodynamic conditions* [33]. From thermodynamic considerations, at temperatures lower than the eutectoid and at high hydrogen concentrations, the reduction step of magnetite to wüstite is favored (red dashed line in Fig. 2), but should be followed by the reduction of wüstite to iron. The reduction of magnetite may be accompanied by the formation of metastable wüstite away from the thermodynamic equilibrium for kinetic considerations. The authors also proposed the formation through the upgrade of the crystal structure.

In contradiction to the previous observations, Jozwiak et al. [35] also performed XRD measurements during the reduction of hematite, but did not identify wüstite below 570 °C. The authors nevertheless suggested the possible formation of wüstite as an intermediate, at least at the interface region between Fe_3O_4 and Fe. The non-presence of wüstite could be explained by the fact that the reduction experiments were performed at much lower reduction rates (lower hydrogen concentrations and gas flow rates), thus under reversible thermodynamic conditions, or due to a lower accuracy of the diffractometer.

Zieliński et al. [43] identified a *considerable quantity* of wüstite in an ex situ measurement of hematite reduced up to 561 °C in the presence of water vapor. Their spectrum also suggested a wüstite closer to the stoichiometric ratio than the one formed after the eutectoid temperature. Since their XRD measurements in dry atmospheres did not reveal the presence of wüstite, we can conclude that the water inhibits the reduction of magnetite to iron and/or wüstite to iron more than the reduction of magnetite to wüstite. As mentioned above, the inhibition of

the reduction of magnetite to iron was clearly demonstrated by Lorente et al. [39] with isothermal runs at 400 °C with varying amounts of added water. The reduction of hematite to magnetite is barely hindered by the presence of water. The reduction of magnetite to iron is completely inhibited by the presence of 10% of water in hydrogen.

Isothermal TG analyses conducted above the eutectoid temperature show less complex profiles. According to Pineau et al. and their XRD measurements, hematite turns stepwise into magnetite, wüstite and iron. Plateaus between two steps may be more or less pronounced. Certain curves [41,44] do not allow identification between successive steps, which may be associated with a diffusion limited process.

The most complex experiments might be those with linear heating rates that exhibit a partial reduction of the sample at the eutectoid temperature. The TPR curves exhibit 3 peaks of varying importance. The first one is always associated with the formation of magnetite from hematite reduction. Around the eutectoid temperature though, a certain amount of magnetite has been reduced to give iron, but traces up to considerable amounts of wüstite can also form. This point is usually followed by a loss of reactivity and then a third peak from the reduction of wüstite to iron. The following explanations can be given for the loss of reactivity between the second and third peaks: 1) The reduction follows the two-step process, magnetite to wüstite, wüstite to iron, and the rate of these reactions is lower than the single step, magnetite to iron. 2) Magnetite and iron recombine into wüstite, and these iron sites acted as a catalyst for the reduction.

Further in situ XRD experiments by Jozwiak et al. [35] shed light on the wüstite disproportionation reaction. Starting from a wüstite sample at room temperature, they conducted two experiments under a linear heating rate, one in an inert atmosphere and one with hydrogen. Under inert conditions, wüstite decomposed progressively and partially into magnetite and iron up to the eutectoid temperature, but recombined rapidly and entirely thereafter. In the reducing atmosphere, the previous disproportionation occurred in parallel with the reduction. The authors derived a phase composition from the XRD patterns. It shows that the disproportionation is almost negligible below 300 °C. Then the amount of wüstite decreases while that of iron and magnetite increases up to 500 °C. After this temperature, the reduction of magnetite, and potentially of wüstite, becomes important, so that the amount of magnetite stays almost constant and the one of iron increases. The magnetite left over after the eutectoid temperature quickly disappears by recombination of magnetite and iron into wüstite and by reduction to wüstite. This results in a spike in the curve of wüstite, which is then further slowly reduced to 900 °C.

As a summary and based on the publications reviewed, we can propose the following chemical scheme for the reduction of hematite powder with hydrogen:

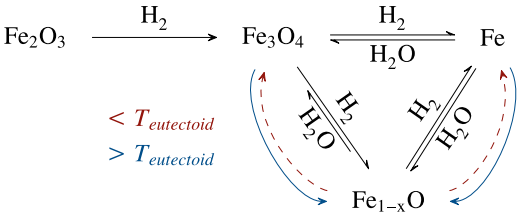

(16)

The black arrows represent the reduction reactions with hydrogen and the reverse oxidation reactions with water. The blue and red lines symbolize the disproportionation reaction of wüstite or its recombination into magnetite and iron.

The first step $Fe_2O_3 \longrightarrow Fe_3O_4$ is written without a backward arrow, because water will eventually slow down this reaction, but will not prevent it. It has the lowest water sensitivity but has a high dependence on the temperature and particle characteristics. Particle size and surface area are important factors in this reduction step. For a given sample, the temperature range of reduction is narrow, indicating a higher activation energy than the successive steps. As a consequence, experiments performed at very low temperatures or low heating rates retard the first step more, which can become rate limiting and lead to the apparent reaction $Fe_2O_3 \longrightarrow Fe$.

The second step is by contrast less sensitive to particle characteristics and temperature, but is severely hindered by water, thus written $Fe_3O_4 \leftrightarrow Fe$. In many TGA and TPR setups, the reaction proceeds to completion below the eutectoid temperature and the wüstite route is not needed to explain the experimental observations. Several authors have detected traces of near-stoichiometric wüstite, but its formation and role in the reduction are not clearly defined, and the integral curves (linear or isothermal) show only one inflection point, between the first and second steps. The presence of wüstite, and further experiments by Jozwiak et al. [35] demonstrate the relative importance of the disproportionation reaction $Fe_{1-x}O \longrightarrow Fe_3O_4 + Fe$, which is therefore marked with dashed lines in Equation (16).

Linear runs featuring unfavorable conditions go stepwise to magnetite and iron up to the eutectoid temperature, then proceed through the wüstite route $Fe_3O_4 \leftrightarrow Fe_{1-x}O \leftrightarrow Fe$. By unfavorable conditions is meant, among others, high mass and low flow rate. In addition to possible thermal gradients or low gas-solid contact, the use of high mass in iron oxide reduction applications increases the amount of water vapor, which is slowly flushed out at a low flow rate. Considering the TPR or TGA furnace as a continuous stirred tank reactor, it is easy to demonstrate that the concentration of water is proportional to the mass of solid reactant and inversely proportional to the flow rate. Therefore, the reduction is spread over a wide temperature range; it starts early as there is initially no water in the furnace, but then an equilibrium is reached, mostly conditioned by how fast the water is flushed out. Under these conditions, no intrinsic chemistry data of the forward rate can be expected, rather an apparent rate embedding the reverse reaction. Near the eutectoid temperature, the sample contains magnetite, iron and a fraction of wüstite. After the eutectoid temperature, the reduction rate decreases, which can be attributed to the recombination of the unreduced magnetite with iron, $Fe_3O_4 + Fe \longrightarrow Fe_{1-x}O$, and the lowest reduction reactivity of wüstite $Fe_{1-x}O \leftrightarrow Fe$.

The experiments performed with water in the gas feed can also be understood in the light of the chemical scheme of Equation (16). A first well-separated peak is observed because after the hematite reduction, the oxidation reaction of iron to magnetite is stronger than the reduction. The reduction continues at higher temperatures when the forward rates finally overcome the backward rates, suggesting a higher activation energy of the reduction reactions than of the oxidation reactions. Under very high H_2/H_2O conditions, the reduction proceeds through the wüstite route, even at temperatures lower than the eutectoid. This suggests that the reduction $Fe_3O_4 \leftrightarrow Fe_{1-x}O$ is less hindered by water than the direct reduction of magnetite to iron. The backward reaction is therefore written with a shorter arrow.

6. Kinetic models

Table 4 summarizes the kinetic models proposed in the literature. As it can be seen, there is a large discrepancy between authors regarding the kinetic parameters and the reaction model for the individual steps.

Most of the works listed in the table assume the validity of the following equation:

$$\frac{d\alpha}{dt} = f(\alpha)k(T), \tag{17}$$

where α is the extent or degree of conversion of the reaction and $f(\alpha)$ is the reaction model. The rate constant $k(T)$, which represents the dependence of the process rate on temperature, is typically expressed by the Arrhenius equation, giving:

$$\frac{d\alpha}{dt} = f(\alpha)A\exp\left(-\frac{E_a}{RT}\right). \tag{18}$$

Table 4
Main chemical reaction steps and their temperature range of validity, as well as proposed activation energy, reaction model and the method of obtention .

Publication	Step & temperature range [°C]	Ea [kJ/mol]	Reaction model	Method
Pineau et al. [33]	$Fe_2O_3 \xrightarrow{x} Fe_3O_4$	75.9 ; 94.8		$\ln(d\alpha/dT)$ *vs.* T_{exp}
2006	$Fe_3O_4 \xrightarrow{x-450} Fe$	87.5 ; 103	2–3 dimensional growth of nuclei	$\ln(d\alpha/dT)$ *vs.* T_{exp}
	$Fe_3O_4 \xrightarrow{450-570} Fe_3O_4 + FeO + Fe$	39.0 ; 35.9	Phase boundary reaction (∞ slabs)	$\ln(d\alpha/dT)$ *vs.* T_{exp}
	$Fe_3O_4 \longrightarrow^{570-x} FeO \longrightarrow^{570-x} Fe$	39.0 ; 35.9	2–3 dimensional growth of nuclei	$\ln(d\alpha/dT)$ *vs.* T_{exp}
Pineau et al. [34]	$Fe_3O_4 \xrightarrow{x-390} Fe$	200 ; 71 ; ...	Phase boundary	$\ln(d\alpha/dT)$ *vs.* T_{exp}
2007	$Fe_3O_4 \xrightarrow{390-570} Fe_3O_4 + FeO + Fe$	44; ...	two-dimensional growth of nuclei	$\ln(d\alpha/dT)$ *vs.* T_{exp}
	$Fe_3O_4 \longrightarrow^{570-x} FeO \longrightarrow^{570-x} Fe$		Diffusion	
Jozwiak et al. [35]	$Fe_2O_3 \xrightarrow{x} Fe_3O_4$	70		$\ln(\beta/T_{max}^2)$ *vs.* $1/T_{max}$
2007	$Fe_3O_4 \xrightarrow{x-570} Fe$	52 ; 55	self-catalyzed nucleation	$\ln(\beta/T_{max}^2)$ *vs.* $1/T_{max}$
	$FeO \xrightarrow{x} Fe$	104		$\ln(\beta/T_{max}^2)$ *vs.* $1/T_{max}$
Tiernan et al. [36]	$Fe_2O_3 \xrightarrow{x} Fe_3O_4$	105.3		$\ln(\beta/T_{max}^2)$ *vs.* $1/T_{max}$
2001	$Fe_3O_4 \xrightarrow{x} Fe$	53.6 ; 64.3		$\ln(\beta/T_{max}^2)$ *vs.* $1/T_{max}$
	$Fe_2O_3 \xrightarrow{x} Fe_3O_4$	96	*n*th-order ; phase boundary	CRTA Equation
	$Fe_3O_4 \xrightarrow{x} Fe$	69–59 ; 75–61	Random nucleation ; autocatalytic	CRTA Equation
Shimokawabe et al. [37]	$Fe_2O_3 \xrightarrow{x} Fe_3O_4$	74.0 ; 117.6	Avrami–Erofeev's equation	$\ln(k)$ *vs.* $1/T_{exp}$
1979	$Fe_3O_4 \xrightarrow{x} Fe$	59.8 ; 72.8	Mampel's equation	$\ln(k)$ *vs.* $1/T_{exp}$
Peña et al. [38]	$Fe_2O_3 \xrightarrow{x} Fe_3O_4$	115.62	Shrinking core model	Curve fitting
2006	$Fe_3O_4 \xrightarrow{x} Fe$	179.52	Nucleation model	Curve fitting
Lorente et al. [39]	$Fe_2O_3 \xrightarrow{x} Fe_3O_4$			
2011	$Fe_3O_4 \xrightarrow{x} Fe$		JMAK	Curve fitting
Wimmers et al. [40]	$Fe_2O_3 \xrightarrow{287-417} Fe_3O_4$	124		$\ln(\beta/T_{max}^2)$ *vs.* $1/T_{max}$
1986	$Fe_3O_4 \xrightarrow{297-477} Fe$	111	three-dimensional nucleation model	$\ln(\beta/T_{max}^2)$ *vs.* $1/T_{max}$
	$FeO \xrightarrow{in\ H_2O} Fe$	172	self-catalyzed	$\ln(\beta/T_{max}^2)$ *vs.* $1/T_{max}$
Piotrowski et al. [41]	$Fe_2O_3 \xrightarrow{700-x} FeO$	28.1	Avrami–Erofe'ev ; Phase-boundary-controlled	Curve fitting
2005				
Hessel et al. [44]	$Fe_3O_3 \xrightarrow{400-500} Fe$		Single phase boundary	Curve fitting
2005	$Fe_2O_3 \xrightarrow{600-900} Fe_3O_4$		Phase boundary	Curve fitting
	$Fe_3O_4 \xrightarrow{600-900} FeO \xrightarrow{600-900} Fe$		Nucleation and growth	Curve fitting

Then, two main groups of methods are used, the isoconversional methods on the one hand and the model-fitting methods on the other hand. In the first group of methods, no determination of the reaction model is needed, hence they are commonly named model-free methods.

Many authors [35,36,40] have used the Kissinger method, one of the model-free methods that can be easily applied to a series of experiments with varying linear heating rates. The method relies on the fact that at the maximum reaction rate of an experiment, the second derivative of the conversion degree with respect to time is zero. Introducing the heating rate β, it results the Kissinger equation:

$$\ln\left(\frac{\beta}{T_{max}^2}\right) = \ln\left(-\frac{AR\,df}{E_a\,d\alpha}\right) - \frac{E_a}{RT_{max}}, \tag{19}$$

where T_{max} is the temperature at which the maximum rate is reached for a given heating rate. Thus, performing a series of experiments with varying linear heating rates should give a straight line when the left hand side of Eq. (19) is plotted against $1/T_{max}$ and the slope yields the activation energy.

Jozwiak et al. [35], Tiernan et al. [36], and Wimmers et al. [40] performed TPR experiments of hematite reduction under pure hydrogen conditions and used the same numerical method, i.e. the Kissinger method, to derive activation energies. Despite these very similar experimental and numerical approaches, the discrepancies in terms of results are large. They found values of 70, 105 and 124 kJ/mol for the step $Fe_2O_3 \longrightarrow Fe_3O_4$ and 52, 54 and 111 kJ/mol for the step $Fe_3O_4 \longrightarrow Fe$.

This method can give us an idea of the activation energies of the reduction steps, but it has important limitations [78]. Some are related to the underlying assumptions of the method. For example, the first term on the right hand side of Eq. (19) must be independent of the heating rate. Another important shortcoming is that the method can adequately represent single-step kinetics only. The base equation, i.e. Eq. (18), has a unique conversion degree and activation energy. Finally, as a graphical method, the results are obtained only by reading a curve, there is no comparison between one kinetic model and the experiments.

Pineau et al. [33,34] also relied on a model-free method to derive activation energies, but applied to isothermal cases. This is even more straightforward as it suffices to take the logarithm of Eq. (18):

$$\ln\left(\frac{d\alpha}{dt}\right) = \ln[f(\alpha)] - \frac{E_a}{RT}. \tag{20}$$

and to plot the left-hand side versus $1/T$ for a series of experiments at different temperatures. This suffers from the same flaws as previously mentioned. In addition, since the term on the left-hand side is not unique for a single experiment, the activation energy is either valid for a certain conversion degree, E_a^{α} or approximated on a certain range of the conversion degree $E_a^{\alpha_1-\alpha_2}$.

In the second group, i.e. in the model-fitting methods, an assumption of the mathematical expression for the reaction model $f(\alpha)$ is needed. The large variety of vocabularies used in the selected literature and reported in Table 4 for the same reaction models should be noted. To avoid confusion, the codes proposed by the ICTAC kinetics committee [78] are used. *Two/three-dimensional growth of nuclei* [33], *Two/three-dimensional nucleation according to Avrami-Erofeev* [40], *Avrami Erofeev's equation on the basis of the random nucleation mechanism* [37], and *Avrami or nucleation model* [38] refer to the following equations for the reaction model:

$$f(\alpha) = 2(1-\alpha)[-\ln(1-\alpha)]^{1/2}, \tag{21}$$

$$f(\alpha) = 3(1-\alpha)[-\ln(1-\alpha)]^{2/3}, \tag{22}$$

corresponding to the designation codes A2 and A3 in Vyazovkin et al.

[78]. Similarly, *phase-boundary-controlled reaction (contracting cylinder/sphere)* [33], *two/three-dimensional phase boundary* [40], *boundary-controlled (nth-order processes)* [36], and *shrinking core model* [38] were employed for the following reaction models:

$$f(\alpha) = 2(1-\alpha)^{1/2}, \tag{23}$$

$$f(\alpha) = 3(1-\alpha)^{2/3}, \tag{24}$$

with codes R2 and R3 [78]. Similarly, Pineau et al. [33] suggested a *phase-boundary-controlled reaction contracting slabs* model, which is not listed by ICTAC but can be found in another publication denoted *zero order* [79] or F0:

$$f(\alpha) = 1. \tag{25}$$

On the other hand, the first order model F1:

$$f(\alpha) = 1-\alpha. \tag{26}$$

is denoted *Random nucleation; unimolecular decay law (first-order)* [33], *unimolecular decay* [40], or *Mampel* [78]. Shimokawabe et al. [37] used the name *Mampel* while referring to the A3 model. Many authors also suggested an *autocatalytic mechanism* [36], *self-catalyzed nucleation* [35], or *self-catalyzed nuclei formation (autocatalysis)* [40], but without giving a mathematical expression. Wimmers et al. [40] associated this mechanism to a power law, but autocatalysis phenomena have a sigmoidal profile rather than accelerating [78], as models P2–P4. Finally, a *two--dimensional diffusion* has been proposed at high temperatures by Pineau et al. [34] whose associated code is D2 [78].

To make a claim about one reaction model or another, the authors based their choice on the curve profile of their results, or by testing the mathematical expressions listed above.

A simple reading of the profiles for isothermal data brings information on a possible reaction model [78]. A decelerating profile could be associated with a phase-boundary, a diffusion, or a first order model, while a sigmoidal profile could be described by a nucleation or autocatalysis model. As depicted in Fig. 5, both decelerating and sigmoidal profiles are found for the individual step under the various isothermal conditions. If this is not sufficient to validate a specific reaction model, we can with a certain confidence exclude an accelerating mechanism, i.e. a power law model.

Testing different reaction models can be done in several ways. For isothermal runs, Eq. (17) can be rewritten and integrated:

$$\frac{\mathrm{d}\alpha}{f(\alpha)} = k(T)\mathrm{d}t, \tag{27}$$

$$\int_0^{\alpha} \frac{\mathrm{d}\alpha}{f(\alpha)} = g(\alpha) = k(T)t. \tag{28}$$

Thus, plotting the integral form of the reaction models presented previously versus the time for a single experiment should yield a straight line if the right model is picked. This was the approach of Pineau et al. [33,34] for the step $Fe_3O_4 \longrightarrow Fe$. As most of the models delivered a correlation coefficient greater than 0.99, the authors mentioned that *it is almost arbitrary to choice between these models* [33]. Another illustration of the limitations of this approach: while the low-temperature magnetite reduction profiles showed a clear sigmoidal profile, the authors concluded on a phase boundary model, i.e. a decelerating model. This may be due to the fact that the initial and final parts of the reduction were removed during the data manipulation, thus removing the accelerating and decelerating parts. Shimokawabe et al. [37] also used this approach, but on both reduction steps. After choosing the reaction models, they further took the logarithm of Eq. (28) for several temperatures to derive the activation energies. In their work, the authors actually used two normalized conversion degrees, one for each step. The first conversion degree equals 1 for 11.1% of the measured weight loss, while the second conversion degree equals 0 at 11.1% and 1 at 100%.

This constitutes a better approach when multiple reduction steps are clearly visible. Most of the kinetic data of the hematite-to-magnetite and magnetite-to-iron steps in the literature have been derived from the global conversion degree and are based on Eq. (18). But this equation is only valid for single-step reactions. Multi-step reactions should be described by multi-step rate equations, i.e., each reaction step i has its own extent of conversion α_i [80].

This mathematical imprecision is actually hard to detect in the methods discussed so far, because no comparison is made between experimental data and the kinetic models. All the methods reviewed are based on graphical reading exclusively, this means they generate kinetic data, but the model is not tested. Most of the time, only the activation energy is reported. To better validate a kinetic model, many works have computed kinetic predictions along with the experiments. Taking isothermal runs as an example, we can isolate α from Eq. (28):

$$\alpha = h(kt), \tag{29}$$

where h is a function of k, t, and the expression chosen for the reaction model. An associated challenge is that the right-hand side of the previous equation contains multiple unknowns. One possibility is to use the kinetic data derived by an isoconversional method [40]. Otherwise, a curve fitting operation [38,39,41] is performed to estimate one or more unknown parameters, as reported in Table 4. Being able to directly compare (visually or mathematically) the kinetic model and the experimental data is a clear benefit. The major drawback is the risk of overfitting. Further testing is required to validate or invalidate the proposed models.

In general, we can question the fact that the conventional approaches, model-free or model-fitting methods, are suited for the reduction of iron oxide. We have seen the multitude of cases in the previous sections. The process is inherently associated with the presence of multiple species with different reactivities with hydrogen and water, further depending on the experimental setup and particle characteristics. Instead of directly solving the kinetics on one or several conversion degrees, another approach consists in determining the solid composition over the time. This can be achieved by solving ordinary differential equations on the mass or mole fractions of the individual solid species [81]. This has recently been accomplished in the case of iron oxide reduction [68,69,82]. The advantages of this method for multistep reactions are obvious. While the conversion degree provides no information about the actual content of hematite, magnetite, wüstite, and iron, working on the solid extensive quantities makes it possible to resolve the individual steps.

Because of its greater flexibility, solving a full mechanism might be the best approach to obtain a comprehensive kinetic model, i.e., a model that is not only intended to represent a single TGA experiment, but can be reliably used in more complicated simulation frameworks featuring non-uniform temperatures and gas compositions. The main shortcoming lies in the determination of the kinetic parameters, which is generally performed via a least squares optimization method. In analogy to curve fitting, there is a risk of overfitting. Overfitted models would fail to predict closely any future observations. As developing kinetic models that can reproduce a single data set under very specific conditions is of no use, the proposed models must be firmly anchored in the physics of the system and demonstrate their availability over a wide range of conditions.

To overcome the overfitting problem, one possible development could be to derive physical and chemical parameters from atomic-scale simulations. Density functional theory (DFT) or molecular dynamics allow to numerically study the structures and properties of iron and its oxides [83], but also the adsorption behavior of gas species on their surfaces [84,85], surface reduction mechanisms [86], as well as transition states, catalytic effects, molecular dissociation and recombination, activation energies, and charge transport [5]. How to couple the

microscale phenomenon with the macroscale kinetics is still a challenge, but recent progress has been made [87,88].

More generally, more efforts should be put on the description of the physical phenomena at an atomic-scale. A better understanding of the elementary processes at internal phase boundaries can serve the development of more meaningful kinetic models. Edström et al. [89] studied magnetite-iron specimens in nitrogen at temperatures between 600 °C and 1090 °C. Iron and magnetite formed layers of wüstite and through the use of markers, they showed that the mass transport was accomplished by the migration of iron across dense wüstite layer. This comforted their previous study [73] where they claimed once a wüstite layer has formed around a hematite or magnetite sample, the reduction proceed by the elementary processes of diffusion through the solid phases and by reactions at the solid phase boundaries. Feilmayr et al. [90] suggested that in the case of hematite reduction into magnetite, iron cations and electrons diffuse through the magnetite layer to the hematite core where they form additional magnetite. Ma et al. [91] further proposed the same mechanism at the magnetite/wüstite interface but fundamentally different at the oxide/iron interfaces, based on the work of Kim et al. [92]. In the latter case, oxygen atoms must diffuse from the oxide/iron interface to the iron/gas interface once a dense iron layer forms.

In the field of iron oxidation, the solid-state diffusion is a predominant process. It was shown on iron strips that the growth of the oxide layers is ruled by the lattice diffusion of ions following Wagners theory; the reaction at the interfaces is not limiting the process [93]. This was recently extended to the oxidation of iron particles [94]. According to Edström [89], there is a close relationship between the oxidation of iron and the reduction of iron oxide. However, in the reduction process, *porosities give rise to smaller dense layers and thus a higher rate of mass transport is accomplished.* This could explain why the solid state-diffusion has received less considerations than in the oxidation process. Future works are needed to determine to which extend and in which cases this can be rate-limiting.

7. Conclusions

Many studies have dealt with the hydrogen reduction of micron-sized iron oxide particles using a thermogravimetric analyzer or via temperature-programmed reduction. In total, 176 unique reduction experiments have been reported in this review. Because of its importance in a variety of applications, there is no doubt that further studies on this topic will be published. This paper aims to serve as a basis and give orientation for further investigation.

The first section dealt with the thermodynamics of the iron/iron oxide system with hydrogen. Many aspects of the reduction process can be explained on the basis of the phase diagram. There is however a certain degree of uncertainty in the thermodynamic data. The latest data for iron, hematite, and magnetite should be used. Wüstite is a more complex compound and simplifications are usually made regarding its composition and the eutectoid temperature.

This review later focused on thermal analysis studies of iron oxide powder reduction with hydrogen. Major discrepancies in the experimental observations have been reported by the authors. For example, one, two, or three peaks can be observed in TPR experiments. Depending on the conditions, the reduction can as well be complete at 400 °C or incomplete at 800 °C. This has been summarized with the help of characteristic curves. To some extent, the discrepancies can be attributed to the particle characteristics, but mostly, we can explain this by the specificity of iron oxide reduction to be delayed by the product of reaction. As noted by Jozwiak et al. [35], *water is the inevitable product […] and may radically change position and shape of the recorded TPR profile.* Therefore, the results of thermal analysis are very sensitive to the experimental setup. To limit the presence of water in the TGA or TPR furnace, we can highly recommend to use a low sample mass and a high gas flow rate. The information provided by the authors is generally too sparse. Giving the dimensions of the furnace, for example, would permit to calculate the superficial velocity, which might be a better indicator than the volumetric gas flow rate. The effect of parameters, such as the crucible shape or the flow configuration should also be further investigated.

Another section briefly presented the current knowledge on the influence of the particle characteristics on the reduction. Here as well research efforts should be pursued. Data at hand seem to indicate a strong influence of the hematite properties on its reduction to magnetite, however, the formed magnetite has a more constant reactivity. Not only the initial particle characteristics, but also their evolution during the reduction play a role. Higher temperatures always favor the initial reaction rates, but increase the risk of sintering, eventually leading to incomplete reduction. The next section led to the development of a general reaction scheme capable of addressing all the experimental observations. It relates the main reduction steps and their dependence on water vapor, but also includes the disproportionation/recombination reactions. Some authors have reported the presence of wüstite below the eutectoid temperature, while others did not find any trace. The mechanism of formation of wüstite and its importance in the reduction should be better understood.

Finally, the proposed kinetic models were systematically reviewed. Models of varying complexity have been proposed, but they are contradictory and none supersedes the others. According to Vrhegyi [95], a good kinetic model should fulfill 4 criteria: description of the behavior of the samples in a wide range of experimental conditions, prediction of the behavior outside the domain of the given set of observations, characteristics that can reveal similarities and differences between the samples, and a deeper insight into the processes taking place. Future works should not only propose a novel kinetic model, but also demonstrate that it is comprehensive enough to be considered a good model.

Declaration of Competing Interest

The authors declare that they have no known competing financial interests or personal relationships that could have appeared to influence the work reported in this paper.

Acknowledgments

This work was performed within the DLR project IronCircle® and the cluster project Clean Circles.

References

[1] F. Patisson, O. Mirgaux, Hydrogen ironmaking: how it works, Metals 10 (2020) 922, https://doi.org/10.3390/met10070922.
[2] Clarivate Web of Science. ©Copyright Clarivate 2022. All rights reserved., 2023, https://www.webofscience.com/.
[3] A. Heidari, N. Niknahad, M. Iljana, T. Fabritius, A review on the kinetics of iron ore reduction by hydrogen, Materials 14 (2021), https://doi.org/10.3390/ma14247540.
[4] D. Spreitzer, J. Schenk, Reduction of iron oxides with hydrogen—A review, Steel Res. Int. 90 (2019) 1900108, https://doi.org/10.1002/srin.201900108.
[5] K. Ma, J. Deng, G. Wang, Q. Zhou, J. Xu, Utilization and impacts of hydrogen in the ironmaking processes: a review from lab-scale basics to industrial practices, Int. J. Hydrog. Energy 46 (52) (2021) 26646–26664, https://doi.org/10.1016/j.ijhydene.2021.05.095.
[6] A.Z. Ghadi, M.S. Valipour, S.M. Vahedi, H.Y. Sohn, A review on the modeling of gaseous reduction of iron oxide pellets, Steel Res. Int. 91 (1) (2020) 1900270, https://doi.org/10.1002/srin.201900270.
[7] P. Wang, M. Ryberg, Y. Yang, K. Feng, S. Kara, M. Hauschild, W.-Q. Chen, Efficiency stagnation in global steel production urges joint supply- and demand-side mitigation efforts, Nat. Commun. 12 (1) (2021) 11, https://doi.org/10.1038/s41467-021-22245-6.
[8] A. Otto, M. Robinius, T. Grube, S. Schiebahn, A. Praktiknjo, D. Stolten, Power-to-steel: reducing CO_2 through the integration of renewable energy and hydrogen into the German steel industry, Energies 10 (4) (2017) 451, https://doi.org/10.3390/en10040451.
[9] Z. Yu, Y. Yang, S. Yang, Q. Zhang, J. Zhao, Y. Fang, X. Hao, G. Guan, Iron-based oxygen carriers in chemical looping conversions: a review, Carbon Resour. Convers. 2 (1) (2019) 23–34, https://doi.org/10.1016/j.crcon.2018.11.004.

[10] J. Adánez, L.F. de Diego, F. García-Labiano, P. Gayán, A. Abad, J.M. Palacios, Selection of oxygen carriers for chemical-looping combustion, Energy Fuels 18 (2) (2004) 371–377, https://doi.org/10.1021/ef0301452.

[11] H.-C. Wu, Y. Ku, Enhanced performance of chemical looping combustion of methane with $Fe_2O_3/Al_2O_3/TiO_2$ oxygen carrier, RSC Adv. 8 (2018) 39902–39912, https://doi.org/10.1039/C8RA07863G.

[12] S.C. Bayham, H.R. Kim, D. Wang, A. Tong, L. Zeng, O. McGiveron, M.V. Kathe, E. Chung, W. Wang, A. Wang, A. Majumder, L.-S. Fan, Iron-based coal direct chemical looping combustion process: 200-h continuous operation of a 25-kWth subpilot unit, Energy Fuels 27 (3) (2013) 1347–1356, https://doi.org/10.1021/ef400010s.

[13] M.F. Bleeker, H.J. Veringa, S.R.A. Kersten, Pure hydrogen production from pyrolysis oil using the steam-iron process: effects of temperature and iron oxide conversion in the reduction, Ind. Eng. Chem. 49 (1) (2010) 53–64, https://doi.org/10.1021/ie900530d.

[14] E. Lorente, J. Peña, J. Herguido, Kinetic study of the redox process for separating and storing hydrogen: oxidation stage and ageing of solid, Int. J. Hydrog. Energy 33 (2) (2008) 615–626, https://doi.org/10.1016/j.ijhydene.2007.09.026.

[15] C.D. Bohn, J.P. Cleeton, C.R. Müller, S.Y. Chuang, S.A. Scott, J.S. Dennis, Stabilizing iron oxide used in cycles of reduction and oxidation for hydrogen production, Energy Fuels 24 (7) (2010) 4025–4033, https://doi.org/10.1021/ef100199f.

[16] B. Gamisch, M. Gaderer, B. Dawoud, On the development of thermochemical hydrogen storage: an experimental study of the kinetics of the redox reactions under different operating conditions, Appl. Sci. 11 (2021) 1623, https://doi.org/10.3390/app11041623.

[17] J.-b. Yang, N.-s. Cai, Z.-s. Li, Hydrogen production from the steam-iron process with direct reduction of iron oxide by chemical looping combustion of coal char, Energy Fuels 22 (4) (2008) 2570–2579, https://doi.org/10.1021/ef800014r.

[18] T. Xu, B. Xiao, G. Fu, S. Yang, X. Wang, Chemical looping hydrogen production with modified iron ore as oxygen carriers using biomass pyrolysis gas as fuel, RSC Adv. 9 (2019) 39064–39075, https://doi.org/10.1039/C9RA08936E.

[19] G. Voitic, V. Hacker, Recent advancements in chemical looping water splitting for the production of hydrogen, RSC Adv. 6 (2016) 98267–98296, https://doi.org/10.1039/C6RA21180A.

[20] P. Debiagi, R. Rocha, A. Scholtissek, J. Janicka, C. Hasse, Iron as a sustainable chemical carrier of renewable energy: analysis of opportunities and challenges for retrofitting coal-fired power plants, Renew. Sust. Energy Rev. 165 (2022) 112579, https://doi.org/10.1016/j.rser.2022.112579.

[21] J. Bergthorson, S. Goroshin, M. Soo, P. Julien, J. Palecka, D. Frost, D. Jarvis, Direct combustion of recyclable metal fuels for zero-carbon heat and power, Appl. Energy 160 (2015) 368–382, https://doi.org/10.1016/j.apenergy.2015.09.037.

[22] L. Choisez, N.E. van Rooij, C.J. Hessels, A.K. da Silva, I.R.S. Filho, Y. Ma, P. de Goey, H. Springer, D. Raabe, Phase transformations and microstructure evolution during combustion of iron powder, Acta Mater. 239 (2022) 118261, https://doi.org/10.1016/j.actamat.2022.118261.

[23] J.M. Bergthorson, Recyclable metal fuels for clean and compact zero-carbon power, Prog. Energy Combust. Sci. 68 (2018) 169–196, https://doi.org/10.1016/j.pecs.2018.05.001.

[24] Clean circles, accessed 02 June 2023, https://www.tu-darmstadt.de/clean-circles/about_cc/index.en.jsp.

[25] Green Steel for Europe Consortium, Technology assessment and roadmapping, 2021.

[26] ICF Consulting Services Limited and Fraunhofer ISI, Industrial innovation: pathways to deep decarbonisation of industry, part 1: technology analysis, 2019.

[27] International Energy Agency IEA, Energy technology perspectives 2020, 2020.

[28] H.Y. Sohn, Energy consumption and CO2 emissions in ironmaking and development of a novel flash technology, Metals 10 (1) (2020) 22, https://doi.org/10.3390/met10010054.

[29] H.Y. Sohn, D.-Q. Fan, A. Abdelghany, Design of novel flash ironmaking reactors for greatly reduced energy consumption and CO2 emissions, Metals 11 (2) (2021) 26, https://doi.org/10.3390/met11020332.

[30] J.L. Schenk, Recent status of fluidized bed technologies for producing iron input materials for steelmaking, Particuology 9 (1) (2011) 14–23, https://doi.org/10.1016/j.partic.2010.08.011.

[31] S.-H. Yi, M.-E. Choi, D.-H. Kim, C.-K. Ko, W.-I. Park, S.-Y. Kim, Finex®as an environmentally sustainable ironmaking process, Ironmak. Steelmak. 46 (7) (2019) 625–631, https://doi.org/10.1080/03019233.2019.1641682.

[32] J. Neumann, E. Corbean, F. Dammel, S. Ulbrich, P. Stephan, Energy and exergy assessment of renewable energy storage using iron as energy carrier. Proceedings of ECOS 2022, Darmstadt, 2022, p. 13.10.26083/tuprints-00022982

[33] A. Pineau, N. Kanari, I. Gaballah, Kinetics of reduction of iron oxides by H_2 part I: low temperature reduction of hematite, Thermochim. Acta 447 (1) (2006) 89–100, https://doi.org/10.1016/j.tca.2005.10.004.

[34] A. Pineau, N. Kanari, I. Gaballah, Kinetics of reduction of iron oxides by H_2part II. Low temperature reduction of magnetite, Thermochim. Acta 456 (2007) 75–77, https://doi.org/10.1016/j.tca.2007.01.014.

[35] W. Jozwiak, E. Kaczmarek, T. Maniecki, W. Ignaczak, W. Maniukiewicz, Reduction behavior of iron oxides in hydrogen and carbon monoxide atmospheres, Appl. Catal., A 326 (1) (2007) 17–27, https://doi.org/10.1016/j.apcata.2007.03.021.

[36] M.J. Tiernan, P.A. Barnes, G.M.B. Parkes, Reduction of iron oxide catalysts: the investigation of kinetic parameters using rate perturbation and linear heating thermoanalytical techniques, J. Phys. Chem. B 105 (1) (2001) 220–228, https://doi.org/10.1021/jp003189+.

[37] M. Shimokawabe, R. Furuichi, T. Ishii, Influence of the preparation history of α-Fe_2O_3 on its reactivity for hydrogen reduction, Thermochim. Acta 28 (2) (1979) 287–305, https://doi.org/10.1016/0040-6031(79)85133-3.

[38] J. Peña, E. Lorente, E. Romero, J. Herguido, Kinetic study of the redox process for storing hydrogen: reduction stage, Catal. Today 116 (3) (2006) 439–444, https://doi.org/10.1016/j.cattod.2006.05.068.2nd European Hydrogen Energy Conference

[39] E. Lorente, J. Herguido, J.A. Peña, Steam-iron process: influence of steam on the kinetics of iron oxide reduction, Int. J. Hydrog. Energy 36 (21) (2011) 13425–13434, https://doi.org/10.1016/j.ijhydene.2011.07.111.

[40] O.J. Wimmers, P. Arnoldy, J.A. Moulijn, Determination of the reduction mechanism by temperature-programmed reduction: application to small iron oxide (Fe_2O_3) particles, J. Phys. Chem. 90 (7) (1986) 1331–1337, https://doi.org/10.1021/j100398a025.

[41] K. Piotrowski, K. Mondal, H. Lorethova, L. Stonawski, T. Szymański, T. Wiltowski, Effect of gas composition on the kinetics of iron oxide reduction in a hydrogen production process, Int. J. Hydrog. Energy 30 (15) (2005) 1543–1554, https://doi.org/10.1016/j.ijhydene.2004.10.013.

[42] R. Viswanath, B. Viswanathan, M. Sastri, Hydrogen spillover effects in the reduction of iron oxide, React. Kinet. Catal. Lett. 2 (1975) 51–56, https://doi.org/10.1007/BF02060952.

[43] J. Zieliński, I. Zglinicka, L. Znak, Z. Kaszkur, Reduction of Fe_2O_3 with hydrogen, Appl. Catal. A 381 (2010) 191–196, https://doi.org/10.1016/j.apcata.2010.04.003.

[44] C. Hessels, T. Homan, N. Deen, Y. Tang, Reduction kinetics of combusted iron powder using hydrogen, Powder Technol. 407 (2022) 117540, https://doi.org/10.1016/j.powtec.2022.117540.

[45] D. Spreitzer, J. Schenk, Iron ore reduction by hydrogen using a laboratory scale fluidized bed reactor: kinetic investigation–experimental setup and method for determination, Metall. Mater. Trans. B 50 (2019), https://doi.org/10.1007/s11663-019-01650-9.

[46] Q. Tang, K. Huang, Determining the kinetic rate constants of Fe_3O_4-to-Fe and FeO-to-Fe reduction by H_2, Chem. Eng. J. 434 (2022) 134771, https://doi.org/10.1016/j.cej.2022.134771.

[47] M. Chase, NIST-JANAF Thermochemical Tables, American Institute of Physics, 1998.-1

[48] P. Linstrom, NIST chemistry webbook, NIST standard reference database 69, 1997, http://webbook.nist.gov/chemistry/. 10.18434/T4D303.

[49] OECD and Nuclear Energy Agency, Chemical Thermodynamics of Iron vol. 13/1, OECD Publishing, Paris, 2014, https://doi.org/10.1787/g2g3f031-en.

[50] P.D. Desai, Thermodynamic properties of iron and silicon, J. Phys. Chem. Ref. Data 15 (3) (1986) 967–983, https://doi.org/10.1063/1.555761.

[51] G.P. Smith, D.M. Golden, M. Frenklach, N.W. Moriarty, B. Eiteneer, M. Goldenberg, C.T. Bowman, R.K. Hanson, S. Song, W.C. Gardiner Jr, V.V. Lissianski, Z. Qin, Gri-mech 3.0, accessed 02 June 2023, http://combustion.berkeley.edu/gri-mech/version30/text30.html.

[52] B.J. McBride, S. Gordon, M.A. Reno, Coefficients for Calculating Thermodynamic and Transport Properties of Individual Species, NASA-TM-4513. Technical Report, National Aeronautics and Space Administration, Office of Management, Scientific and Technical Information Program, Washington, DC, 1993.https://ntrs.nasa.gov/search.jsp?R=19940013151

[53] P. Spencer, O. Kubaschewski, A thermodynamic assessment of the iron-oxygen system, Calphad 2 (2) (1978) 147–167, https://doi.org/10.1016/0364-5916(78)90032-9.

[54] B. Sundman, An assessment of the Fe–O system, J. Phase Equilib. 12 (1991) 127–140.

[55] F. Grønvold, S. Stølen, P. Tolmach, E.F. Westrum, Heat capacities of the wüstites Fe0.9379O and Fe0.9254O at temperatures *T* from 5 K to 350 K. Thermodynamics of the reactions: xfe(s) + (1/4)fe3o4(s) = fe0.7500+xo(s) = fe1-yo(s) at t≈ 850 k, and properties of fe1-yo(s) to t = 1000 k. thermodynamics of formation of wüstite, J. Chem. Thermodyn. 25 (9) (1993) 1089–1117, https://doi.org/10.1006/jcht.1993.1107.

[56] R. Beheshti, J. Moosberg-Bustnes, R.E. Aune, Modeling and simulation of isothermal reduction of a single hematite pellet in gas mixtures of H_2 and CO. TMS 2014: 143rd Annual Meeting & Exhibition, Springer, Cham, Switzerland, 2016, pp. 495–502.

[57] O. Teplov, Kinetics of the low-temperature hydrogen reduction of magnetite concentrates, Russ. Metall. 2012 (2012), https://doi.org/10.1134/S0036029512010132.

[58] D. Spreitzer, J. Schenk, Fluidization behavior and reducibility of iron ore fines during hydrogen-induced fluidized bed reduction, Particuology 52 (2020) 36–46, https://doi.org/10.1016/j.partic.2019.11.006.

[59] T.S.T. Saharuddin, A. Samsuri, F. Salleh, R. Othaman, M.B. Kassim, M. W. Mohamed Hisham, M.A. Yarmo, Studies on reduction of chromium doped iron oxide catalyst using hydrogen and various concentration of carbon monoxide, Int. J. Hydrog. Energy 42 (14) (2017) 9077–9086, https://doi.org/10.1016/j.ijhydene.2016.08.151.

[60] M. Sastri, R. Viswanath, B. Viswanathan, Studies on the reduction of iron oxide with hydrogen, Int. J. Hydrog. Energy 7 (12) (1982) 951–955, https://doi.org/10.1016/0360-3199(82)90163-X.

[61] D.N. Drakshayani, R.M. Mallya, Reactivity with hydrogen of pure iron oxide and of iron oxides doped with oxides of Mn, Co, Ni and Cu, J. Therm. Anal. 37 (5) (1991) 891–906, https://doi.org/10.1007/bf01932787.

[62] M. Kazemi, B. Glaser, D. Sichen, Study on direct reduction of hematite pellets using a new TG setup, Steel Res. Int. 85, (2014) 718–728, https://doi.org/10.1002/srin.201300197.

[63] M. Kazemi, M.S. Pour, D. Sichen, Experimental and modeling study on reduction of hematite pellets by hydrogen gas, Metall. Mater. Trans. B 48, (2017) 1114–1122, https://doi.org/10.1007/s11663-016-0895-3.
[64] E.T. Turkdogan, J.V. Vinters, Gaseous reduction of iron oxides: part I. Reduction of hematite in hydrogen, Metal. Trans. 2, (1971) 3175–3188, https://doi.org/10.1007/BF02814970.
[65] I.R.S. Filho, H. Springer, Y. Ma, A. Mahajan, C.C. da Silva, M. Kulse, D. Raabe, Green steel at its crossroads: hybrid hydrogen-based reduction of iron ores, 2022, 10.48550/ARXIV.2201.13356.
[66] A. Bonalde, A. Henriquez, M. Manrique, Kinetic analysis of the iron oxide reduction using hydrogen-carbon monoxide mixtures as reducing agent, ISIJ Int. 45, (2005) 1255–1260.
[67] K. Mondal, H. Lorethova, E. Hippo, T. Wiltowski, S. Lalvani, Reduction of iron oxide in carbon monoxide atmosphere–reaction controlled kinetics, Fuel Process. Technol. 86 (1) (2004) 33–47, https://doi.org/10.1016/j.fuproc.2003.12.009.
[68] Q. Fradet, M.L. Ali, U. Riedel, Development of a porous solid model for the direct reduction of iron ore pellets, Steel Res. Int. 93 (12) (2022) 2200042, https://doi.org/10.1002/srin.202200042.
[69] M.L. Ali, Q. Fradet, U. Riedel, Kinetic mechanism development for the direct reduction of single hematite pellets in H_2/CO atmospheres, Steel Res. Int. 93 (12) (2022) 2200043, https://doi.org/10.1002/srin.202200043.
[70] R. Viswanath, B. Viswanathan, M. Sastri, Kinetics and mechanism of reduction of ferric oxide by hydrogen, Trans. Jpn. 18 (1977) 149–154, https://doi.org/10.2320/matertrans1960.18.149.
[71] N. Towhidi, Reduction kinetics of commercial low-silica hematite pellets with CO-H_2 mixtures over temperature range 600–1234 °C, Ironmak. Steelmak. 6, (1981) 237–249.
[72] E.T. Turkdogan, J.V. Vinters, Gaseous reduction of iron oxides: part III. Reduction-oxidation of porous and dense iron oxides and iron, Metall. Mater. Trans. B 3 (6) (1972) 1561–1574, https://doi.org/10.1007/BF02643047.
[73] J.O. Edström, The mechanism of reduction of iron oxides, J. Iron Steel Res. Int. 175, (1953) 289–304.
[74] Y. Bai, J.R. Mianroodi, Y. Ma, A.K. da Silva, B. Svendsen, D. Raabe, Chemo-mechanical phase-field modeling of iron oxide reduction with hydrogen, Acta Mater. 231 (2022) 117899, https://doi.org/10.1016/j.actamat.2022.117899.
[75] A.A. El-Geassy, M.I. Nasr, M.M. Hessien, Effect of reducing gas on the volume change during reduction of iron oxide compacts, ISIJ Int. 36 (6) (1996) 640–649, https://doi.org/10.2355/isijinternational.36.640.
[76] L. Yi, Z. Huang, T. Jiang, L. Wang, T. Qi, Swelling behavior of iron ore pellet reduced by H_2–CO mixtures, Powder Technol. 269 (2015) 290–295, https://doi.org/10.1016/j.powtec.2014.09.018.
[77] Y. Ma, I.R. Souza Filho, X. Zhang, S. Nandy, P. Barriobero-Vila, G. Requena, D. Vogel, M. Rohwerder, D. Ponge, H. Springer, D. Raabe, Hydrogen-based direct reduction of iron oxide at 700 °C: heterogeneity at pellet and microstructure scales, Int. J. Miner. Metall. Mater. 29 (10) (2022) 1901–1907, https://doi.org/10.1007/s12613-022-2440-5.
[78] S. Vyazovkin, A. Burnham, J. Criado, L. Pérez-Maqueda, C. Popescu, N. Sbirrazzuoli, ICTAC kinetics commitee recommendations for performing kinetic computations on thermal analysis data, Thermochim. Acta 520 (2011) 1–19, https://doi.org/10.1016/j.tca.2011.03.034.
[79] L. Fedunik-Hofman, A. Bayon, S.W. Donne, Kinetics of solid-gas reactions and their application to carbonate looping systems, Energies 12 (15) (2019) 1–35, https://doi.org/10.3390/en12152981.
[80] S. Vyazovkin, A.K. Burnham, L. Favergeon, N. Koga, E. Moukhina, L.A. Pérez-Maqueda, N. Sbirrazzuoli, ICTAC kinetics committee recommendations for analysis of multi-step kinetics, Thermochim. Acta 689 (2020) 178597, https://doi.org/10.1016/j.tca.2020.178597.
[81] J.-L. Dirion, C. Reverte, M. Cabassud, Kinetic parameter estimation from TGA: optimal design of TGA experiments, Chem. Eng. Res. Des. 86 (6) (2008) 618–625, https://doi.org/10.1016/j.cherd.2008.02.001.
[82] C. Kuhn, A. Düll, P. Rohlfs, S. Tischer, M. Börnhorst, O. Deutschmann, Iron as recyclable energy carrier: feasibility study and kinetic analysis of iron oxide reduction, Appl. Energy Combust. Sci. 12 (2022) 100096, https://doi.org/10.1016/j.jaecs.2022.100096.
[83] S. Zhang, K. Li, Y. Ma, F. Guo, C. Jiang, Z. Liang, Y. Bu, J. Zhang, Density functional studies on the atomistic structure and properties of iron oxides: a parametric study, Materials 15 (23) (2022) 18, https://doi.org/10.3390/ma15238316.
[84] H. Zhong, L. Wen, J. Li, J. Xu, M. Hu, Z. Yang, The adsorption behaviors of CO and H_2 on FeO surface: a density functional theory study, Powder Technol. 303 (2016) 100–108, https://doi.org/10.1016/j.powtec.2016.09.017.
[85] Q. Cheng, A.N. Conejo, Y. Wang, J. Zhang, A. Zheng, Z. Liu, Adsorption properties of hydrogen with iron oxides (FeO, Fe_2O_3): a ReaxFF molecular dynamics study, Comput. Mater. Sci. 218 (2023) 111926, https://doi.org/10.1016/j.commatsci.2022.111926.
[86] F. Liu, J. Liu, Y. Li, R. Fang, Theoretical study of reduction mechanism of Fe_2O_3 by H_2 during chemical looping combustion, Chin. J. Chem. Eng. 37 (2021) 175–183, https://doi.org/10.1016/j.cjche.2021.02.006.
[87] Z. Li, J. Cai, L. Liu, A first-principles microkinetic rate equation theory for heterogeneous reactions: application to reduction of Fe_2O_3 in chemical looping, Ind. Eng. Chem. Res. 60 (43) (2021) 15514–15524, https://doi.org/10.1021/acs.iecr.1c03214.
[88] Y. Wang, Z. Li, A DFT-based microkinetic theory for Fe_2O_3 reduction by CO in chemical looping, Proc. Combust. Inst. (2022), https://doi.org/10.1016/j.proci.2022.07.026.
[89] J.O. Edstrom, G. Bitsianes, Solid state diffusion in the reduction of magnetite, JOM 7 (6) (1955) 760–765, https://doi.org/10.1007/BF03377566.
[90] C. Feilmayr, A. Thurnhofer, F. Winter, H. Mali, J. Schenk, Reduction behavior of hematite to magnetite under fluidized bed conditions, ISIJ Int. 44 (7) (2004) 1125–1133, https://doi.org/10.2355/isijinternational.44.1125.
[91] Y. Ma, I.R. Souza Filho, Y. Bai, J. Schenk, F. Patisson, A. Beck, J.A. van Bokhoven, M.G. Willinger, K. Li, D. Xie, D. Ponge, S. Zaefferer, B. Gault, J.R. Mianroodi, D. Raabe, Hierarchical nature of hydrogen-based direct reduction of iron oxides, Scr. Mater. 213 (2022) 114571, https://doi.org/10.1016/j.scriptamat.2022.114571.
[92] S.-H. Kim, X. Zhang, Y. Ma, I.R. Souza Filho, K. Schweinar, K. Angenendt, D. Vogel, L.T. Stephenson, A.A. El-Zoka, J.R. Mianroodi, M. Rohwerder, B. Gault, D. Raabe, Influence of microstructure and atomic-scale chemistry on the direct reduction of iron ore with hydrogen at 700 °C, Acta Mater. 212 (2021) 116933, https://doi.org/10.1016/j.actamat.2021.116933.
[93] J. Païdassi, Sur la cinetique de l'oxydation du fer dans l'air dans l'intervalle 700–1250 °C, Acta Metall. 6 (3) (1958) 184–194, https://doi.org/10.1016/0001-6160(58)90006-3.
[94] X. Mi, A. Fujinawa, J.M. Bergthorson, A quantitative analysis of the ignition characteristics of fine iron particles, Combust. Flame 240 (2022) 112011, https://doi.org/10.1016/j.combustflame.2022.112011.
[95] G. Várhegyi, Aims and methods in non-isothermal reaction kinetics, J. Anal. Appl. Pyrolysis 79 (1–2) (2007) 278–288, https://doi.org/10.1016/j.jaap.2007.01.007.